Monitoring and reactive-transport modeling of the spatial and temporal variations of the Strengbach spring hydrochemistry

Julien Ackerer, François Chabaux, Yann Lucas, Alain Clément, Bertrand Fritz, Emilie Beaulieu, Daniel Viville, Pierret Mc, Sophie Gangloff, Philippe Négrel

▶ **To cite this version:**

Julien Ackerer, François Chabaux, Yann Lucas, Alain Clément, Bertrand Fritz, et al.. Monitoring and reactive-transport modeling of the spatial and temporal variations of the Strengbach spring hydrochemistry. Geochimica et Cosmochimica Acta, 2018, 225, pp.17-35. 10.1016/j.gca.2018.01.025 . hal-03885578

HAL Id: hal-03885578
https://hal.science/hal-03885578

Submitted on 5 Dec 2022

HAL is a multi-disciplinary open access archive for the deposit and dissemination of scientific research documents, whether they are published or not. The documents may come from teaching and research institutions in France or abroad, or from public or private research centers.

L'archive ouverte pluridisciplinaire **HAL**, est destinée au dépôt et à la diffusion de documents scientifiques de niveau recherche, publiés ou non, émanant des établissements d'enseignement et de recherche français ou étrangers, des laboratoires publics ou privés.

Monitoring and reactive-transport modeling of the spatial and temporal variations of the Strengbach spring hydrochemistry

Ackerer J .[1], Chabaux F.[1], Lucas Y.[1], Clément A.[1], Fritz B.[1], Beaulieu E.[1], Viville D.[1], Pierret MC[1], Gangloff S.[1], Négrel Ph.[2]

(1) Laboratoire d'Hydrologie et de Géochimie de Strasbourg (UMR 7517), CNRS, Université de Strasbourg, 1 rue Blessig, 67084 Strasbourg cedex, France.

(2) Bureau de Recherches Géologiques et Minières (BRGM), 3 Avenue Claude Guillemin, 45000 Orléans, France.

Abstract:

This study focuses on 20 years of hydrochemical monitoring of the small springs that emerge in the experimental granitic catchment of Strengbach (OHGE, France) and the simulation of these data using the KIRMAT code. The data indicate that the Strengbach springs display chemostatic behavior; that is, limited temporal variations were noted in the concentrations of dissolved silica (H_4SiO_4) and most of the basic cations during the studied period (1987-2010), resulting in relative stability of the global weathering fluxes exported by the springs. Only the Ca^{2+} concentrations reflect a significant decrease in all the Strengbach springs since 1987, and the variations differ from one spring to another. The modeling results show that the decrease in Ca^{2+} in the Strengbach springs is due to the response of the water-rock interactions within the bedrock to the variations in the chemical composition of the soil solutions, which were characterized by a significant increase in pH and a decrease in Ca^{2+} concentrations between 1987 and 2010. The decrease in Ca^{2+} concentrations seen in the Strengbach springs is controlled by changes in the apatite dissolution rate and the compositions of clay minerals induced by the soil solution changes. The differences observed between the Ca^{2+} trends of the springs are related to changes in the residence time of the water supplying the different springs. The weak impact of the soil solution modifications on the dissolution rates of other primary minerals and on the bulk precipitation rates of the clay minerals explains the relative stability over time of the concentrations of the other cations and dissolved silica in the water derived from the Strengbach springs. Further, the hydrochemical simulations suggest that the chemostatic behavior of the Strengbach springs cannot be explained by the mobilization of waters that are close to chemical equilibrium. Finally, a comparison of current and long-term weathering rates determined from the spring water monitoring and a regolith profile shows that the modern chemical fluxes of Ca^{2+} are higher than the long-term ones, whereas the weathering fluxes of H_4SiO_4 and Na^+ have likely been much more stable over time. All of these results indicate that the silicate weathering processes are characterized by weak spatial and temporal variability in the Strengbach catchment, while the chemical elements such as Ca^{2+}, for which the budget in the spring waters is controlled by the dynamic behavior of clay minerals and minor minerals, are significantly affected by Quaternary climatic variations and decennial environmental changes.

Keywords: long-term hydrochemical monitoring, weathering fluxes, reactive-transport modeling, Water-rock interactions, critical zone observatory.

1-Introduction

Continental silicate weathering is one of the major factors that controls the chemical evolution of the Earth's surface. From the large-scale transport of solutes by rivers to the development of regolith on hillslopes, complex relationships and linkages exist between weathering, erosion, vegetation and climate (Egli et al., 2008; Goddéris et al., 2009; Beaulieu et al., 2012; Donnini et al., 2016). Numerical approaches and reactive transport models have become a powerful tool to explore the forces that drive chemical weathering on scales ranging from small watersheds to continentals (Beaulieu et al., 2010; Lebedeva et al., 2010; Goddéris and Brantley, 2013; Li et al., 2014; Schaffhauser et al, 2014). The aim of this study is to illustrate the potential of the hydrochemical approaches at the scale of an elementary watershed, the Strengbach watershed in France. The Strengbach catchment is one of the reference sites for the critical zone observatories in France ("Observatoire Hydrogéochimique de l'Environnement", OHGE, http://ohge.unistra.fr; http://rnbv.ipgp.fr). This experimental catchment is one of the few critical zone observatories in the world where geochemical data on soil solutions, streams, and springs have been collected for 20 years; moreover, mineralogical characterization of the soils and bedrock has been carried out. It is a relevant site where hydrochemical modeling approaches can be applied to study the origin of spatial and temporal variations in the chemical composition of surface waters. The results obtained in this study highlight the interest of this approach in improving our understanding of the main processes controlling the chemical variability of surface waters and providing insights into the sensitivity of weathering processes to recent environmental changes and to Quaternary climatic variations.

2-Site description

The Strengbach catchment is a small watershed (0.8 km²), where multidisciplinary studies have been carried out since 1986 ("Observatoire Hydrogéochimique de l'Environnement", OHGE). It is located in the Vosges Mountains of northeastern France (Figure 1) at altitudes between 883 and 1147 m a.s.l. The current climate is mountainous oceanic. The annual mean temperature is 6 ˚C, the annual mean rainfall is 1400 mm, the annual mean runoff is about 800 mm, and the annual mean evapotranspiration has been estimated to be about 600 mm (Viville et al., 2012). Snowfall occurs from December to March and the major hydrological and high-flow events frequently occur during snowmelt periods at the end of the winter season. A saturated area is situated close to the watershed outlet and is connected to the Strengbach stream. The soils of the watershed, which range from Hyperdystric Cambisols to Entic Podzols (WRB, 2006), are acidic, coarse in texture, and are less than 1 m in thickness. A mixed forest composed of beech and spruce covers up to 90% of the catchment. During the 1980s, the watershed experienced acid atmospheric deposition, and scientific investigations have been conducted to understand the observed tree mortality and the needle yellowing of the spruce stands (Probst et al, 1990; Dambrine et al., 1998). The bedrock is a coarse-grained Hercynian granite that has been affected by hydrothermal events and is characterized by low contents of base cations, especially Ca (Fichter et al., 1998). The granite is strongly hydrothermally altered within the northern part of the watershed, and it is relatively weakly affected by hydrothermal processes on the southern slopes. The hydrothermal events caused a decrease in the abundances of K-feldspar and albite in the granite and promoted the precipitation of quartz, hematite and

fine-grained white mica in veins (El Gh'Mari, 1995). Several small but permanent springs emerge on both hillsides of the catchment (Figure 1).

3-Sample location and data acquisition

This study is based on the data obtained from the hydrochemical monitoring carried out in the Strengbach experimental catchment. More specifically, it focuses on comparing the chemical compositions of several springs emerging in the Strengbach watershed and understanding their geochemical variations during the period between 1990 and 2010. Four springs, the CS springs (Figure 1), are located within the southern part of the Strengbach catchment, where the bedrock is weakly affected by hydrothermal alteration. Each spring sources is a fracture in the granitic bedrock at a depth of 2 to 5 m. These four springs then gather in a single collector (CR). The water that accumulates in this collector is used to supply drinking water to the neighboring village of Aubure. The two other springs (RH3 and ARG) used in this study emerge naturally on the slopes. The RH3 spring is located on the hydrothermally altered northern part of the watershed. The other natural spring, the ARG spring, also lies within the northern part of the watershed, but it occurs near the Strengbach stream (Figure 1). A detailed study of the geochemical variations in the spring and stream waters of the Strengbach watershed can be found in Prunier, (2008) and in Pierret et al. (2014) for the period 2004-2006. These studies analyzed major and trace element concentrations, $^{87}Sr/^{86}Sr$ isotope ratios, and the ($^{234}U/^{238}U$) activity ratios of the waters. The results suggested that each spring is characterized by a rather stable and independent water pathway within the watershed substratum (Pierret et al., 2014), as was also proposed for a neighboring granitic watershed in the Vosges Mountains, the Ringelbach watershed (Schaffhauser et al., 2014). Soil solutions have been sampled from 1992 to 2010 at two

different locations (Figure 1), one at a beech site on the southern slope (the beech stand is locally named HP) and one at a spruce site on the northern slope (the spruce stand is named VP; the data are given in Prunier et al., 2015). All water samples, which represent spring waters, soil solutions and rainwater, were filtered soon after collection with 0.45-µm cellulose acetate membrane filters, stored in cleaned polyethylene bottles and conserved in a cold room until they were analyzed chemically. The analysis of water chemistry was performed by following techniques used at LHyGeS (Strasbourg, France), described by Probst et al. (1990) and Dambrine et al. (1998; for the 1986-1998 period) and by Gangloff et al. (2014; for the samples collected after 2000). In addition, the mineralogical compositions and the petrological properties of two rocks that are representative of the two extreme granitic facies constituting the bedrock of the watershed have been assessed. These rocks include a sample of strongly hydrothermally altered granite, the CA sample, which was collected in the northern part of the watershed, and a granitic sample from the southern slope, the HPT sample, which is weakly affected by hydrothermal processes (Figure 1). Mineralogical and petrological data on these two samples can be found in El Gh'Mari (1995) and are summarized in Table 1. Discharges of water from the springs were also measured regularly. Together with the major element concentrations, these data enable estimation of the dissolved fluxes exported by each spring.

4-Spatial variability and temporal evolution of the spring water chemistry

4-1-Spatial and seasonal variability

The geochemical data obtained from the different springs confirm the occurrence of spatial variations of spring water chemistry at the watershed scale, especially between the northern part of the watershed, which is strongly hydrothermally altered, and the southern slopes,

which are weakly affected by hydrothermal processes. Such variations were highlighted by Pierret et al. (2014) and in Prunier (2008), in that the elemental ratios (i.e., Mg/Na Ca/Na, and K/Na) and Sr isotopic ratios show different values between the two slopes of the watershed. Mg^{2+} differs most strongly between the two slopes, and systematically higher values of this species were noted in the RH3 spring than in the CS springs (Figure 2a). This difference is likely related to the higher Mg content in the hydrothermally altered granite facies, and the presence of gneiss may influence the chemical composition of the source waters in the northern part of the catchment (Fichter et al., 1998; Pierret et al., 2014). Slightly higher concentrations of K^+ and to a lesser extent Ca^{2+} occur in the RH3 spring, which drains the northern part of the catchment. The concentrations of the other species, such as H_4SiO_4, Na^+, and the anions, as well as pH and alkalinity, show some slight differences from one spring to another, with no systematic differences identified between the two hillslopes. For a given spring at the annual timescale, the data indicate relative stability of the silica and cation concentrations under widely varying discharges. Solute concentrations vary in the spring waters by less than 15 %, whereas discharge can vary by more than a factor of 10, implying that concentrations are relatively stable over a wide range of hydrological conditions, and that seasonal fluctuations are relatively limited.

4-2-Long-term inter-annual variability

At the inter-annual timescale, the 20 years of chemical monitoring data reflect systematic trends in the chemical concentrations with time, but not all chemical species are affected, as is well demonstrated by the water samples obtained from the CR collector (Figure 3). Magnitudes of these long-term concentration variations can be different from one spring to another (Figure 4, in Electronic Annex Figure EA1). Species that show the most significant

183 long-term changes in concentrations, with amplitudes much higher than the seasonal
184 fluctuations, include Ca^{2+} (Figure 2b) and (to a lesser extent) Mg^{2+} and K^{+} (Figure 4) and SO_4^{2-}
185 and NO_3^{-} (Figure EA1). Of all these species, SO_4^{2-} is the only one that is characterized by a
186 similar decrease in all the studied spring waters. For cations, the concentration decrease is
187 relatively weak for Mg^{2+} and for K^{+}, but it is much larger for Ca^{2+}, and the magnitude of
188 variation can differ significantly from one spring to another. The decrease in Ca^{2+}
189 concentrations is about 20% for CS3, 25% for CS2 and CS4, and it ranges up to 50% for the
190 CS1 and RH3 springs between 1990 and 2010 (Figure 4). During the same period, pH and
191 alkalinity have tended to increase in the spring waters. For example, an increase in the mean
192 annual pH from approximately 5.80 to 6.40 and an increase in the mean alkalinity from 0.017
193 to 0.030 meq/L were noted for the CS1 spring between 1986 and 2010. The temporal
194 evolution of NO_3^{-} is different than for the other chemical species. NO_3^{-} concentrations are
195 similar for all of the springs in 1990 but show different trends after 2004; significant
196 increases can be seen in some of the CS springs and the RH3 spring (Figure EA1). Cl^{-}, Na^{+}, and
197 H_4SiO_4 are characterized by relatively uniform concentrations within the catchment and by
198 nearly constant concentrations over the studied period (Figure 4; Figure EA1).

199 The long-term trends observed for the major dissolved species in the spring waters can be
200 explained by the relative importance of the lithogenic and atmospheric contributions to the
201 element budgets. The OHGE data indicate that, during the 1986-2010 period, cation and
202 H_4SiO_4 concentrations have been relatively stable in the rainwater collected in the
203 watershed (OHGE data; Figure EA2 and EA3). The Mg^{2+} and H_4SiO_4 concentrations in the
204 rainwater are stable and very low (<0.01 mmol/L). The Ca^{2+} and K^{+} concentrations are
205 relatively stable but higher (<0.03 mmol/L), whereas the concentrations of Na^{+} indicate that
206 Na^{+} is the dominant cation in the rainwater (<0.04 mmol/L). In addition, the pH variations in

207 the rainwater show a significant increasing trend (Figure EA4), with a mean annual pH of
208 4.66 in 1990 and 5.63 in 2010. For the anions, the concentrations of Cl^- and NO_3^- in the
209 rainwater are nearly constant, while the SO_4^{2-} concentrations tend to decrease over the
210 same period (Figure EA3).

211 In this context, and given the extremely low Cl content of the granite, the stability and
212 homogeneity of the concentrations of Cl^- in the spring waters is likely to be simply a
213 consequence of the stable atmospheric deposition. Concerning the decrease in SO_4^{2-}
214 concentrations, which is characterized by a comparable magnitude for each spring, the
215 observation of a simultaneous SO_4^{2-} concentration decrease in the rainwater, and with a
216 similar amplitude, suggests that the variations in the sources are directly induced by the
217 reduction in atmospheric deposition in the watershed from 1986 to 2010. For NO_3^-, the
218 increase cannot be related to any atmospheric increase in NO_3^-, as the NO_3^- concentrations
219 remain stable in the rainwater during the 1986-2010 period (OHGE data, Figure EA3). Rather
220 than a modification of the atmospheric inputs, the nitrogen cycle could have been affected
221 by the recent biomass changes related to the forest decline observed in the watershed. The
222 increase in exported NO_3^- may be explained by the tree mortality observed in some parts of
223 the catchment that was caused by the exceptional drought of 2003 and a recent outbreak of
224 xylophage insects. Similar increases have also been identified in other forested experimental
225 catchments after similar perturbations (Knight et al., 1991; Lovett et al., 2002). The role of
226 vegetation is reinforced by the strong increase in the NO_3^- concentrations seen in some of
227 the soil solution samples collected at the spruce site that cannot be explained by changes in
228 the concentration of NO_3^- in the rainwater, which is stable (OHGE data, Figure EA3). The data
229 therefore suggest that the temporal evolution of the anion concentrations in the spring
230 waters are mainly controlled by atmospheric deposition and vegetation cover changes.

For the cations and dissolved silica, the budget of these species is controlled by water-rock interactions within the bedrock and the atmospheric contribution. The importance of the atmospheric contribution in the Strengbach catchment strongly depends on the species being considered. It is negligible for H_4SiO_4 (<3%), relatively low for Mg^{2+} and Ca^{2+} (<20%), and significant for Na^+ and K^+ (up to 60%; Viville et al., 2012). The fact that each spring shows a different decreasing trend for the Ca^{2+} concentrations indicates that the evolution of Ca^{2+} is not only related to the variability in atmospheric input, as seen for the SO_4^{2-} anion; it also depends on the reactivity of minerals within the bedrock and the hydrodynamic characteristics of each spring. At the same time, the constant and uniform concentrations of H_4SiO_4 and Na^+ and the limited variations in K^+ and Mg^{2+} in the spring water point to the stable functioning of silicate weathering within the bedrock.

4-3-Spatial and temporal variations of the weathering fluxes

Monitoring the geochemical composition and discharge of the Strengbach springs also allows estimation of the chemical weathering fluxes exported by the different springs during the 1986-2010 period. This calculation is performed in this study for dissolved silica (H_4SiO_4) and basic cations (K^+, Na^+, Ca^{2+} and Mg^{2+}) using the instantaneous spring water discharges and the elemental concentrations. The conversion of the net chemical fluxes into specific weathering fluxes (in T/km²/yr) requires the accurate estimation of the surface areas drained by the different springs and correct for the atmospheric contributions. This was done by Viville et al. (2012) for the Strengbach stream at the outlet of the catchment. This is done in this study for the different springs. The surface areas drained by the Strengbach springs are assimilated to the small surface areas of the “watersheds” defined by the different springs. The correction of the atmospheric contribution, including the effect of throughfalls and/or

biomass storage on the chemical fluxes carried by the different springs, has been made following the approach detailed in Viville et al. (2012) for the whole watershed. The calculated weathering fluxes indicate that from 1986 to 2010, the only chemical fluxes that vary significantly with time at a decadal scale and from one spring to another are the Ca^{2+} fluxes. In accordance to the elemental concentration variations, the H_4SiO_4 and Na^+ weathering fluxes are relatively stables over the studied period. The weathering flux variations therefore suggest that the recent perturbations recorded in the catchment have not modified all the primary mineral weathering rates; instead, they may have affected only Ca-rich minerals, such as apatite, and/or the compositions of the clay minerals. To evaluate these hypotheses in a quantitative manner, a numerical modeling approach has been developed to capture the main processes involved in the acquisition and the evolution of the chemistry of the Strengbach springs. The modeling will focus on the dissolved silica and the cation concentrations and will be based on the mean annual data from 1990 to 2010.

5-Hydrochemical modeling

5-1-KIRMAT model description

The hydrochemical simulations performed in this study employ the 1D thermo-kinetic code KIRMAT (KInetic Reactions and MAss Transport; Gérard, 1996; Gérard et al., 1998). The KIRMAT code simultaneously solves equations describing geochemical reactions and transport mass balances in a saturated porous medium. Mass transport comprises the effects of convection, diffusion and kinematic dispersion. Chemical reactions include the dissolution of primary minerals and oxidoreduction reactions, as well as the precipitation of secondary minerals and clays. Dissolution and precipitation rate calculations are based on

the kinetic laws derived from transition state theory (Eyring, 1935; Murphy and Helgeson, 1987). The dissolution rate of a mineral is expressed in KIRMAT as follows (Ngo et al., 2014):

$$r_d = k_d * S_m^{eff} * \alpha_{H^+}^n * \left(1 - \left(\frac{Q_m}{K_m}\right)^{n1}\right)^{n2} \quad (1)$$

where k_d is the dissolution rate constant (mol/m²/yr), S_m^{eff} is the reactive surface of the mineral m (m²/kg H_2O), $\alpha_{H^+}^n$ is the activity of protons, Q_m is the ion activity product of the mineral m, K_m is the thermodynamic equilibrium constant of the hydrolysis reaction of the mineral m, and $n1$ and $n2$ are exponents that depend on the pH of the solution (Ngo et al., 2014). To take into account the ionic exchange between water and clays, the clay fraction is defined in KIRMAT as a solid solution (Tardy and Fritz, 1981). The clay solid solution is precipitated at thermodynamic equilibrium and is made up of a combination of pure clay end members. Its composition varies with time, depending on the evolution of the water chemistry and the bedrock mineralogy during the simulation (Gérard, 1996; Schaffhauser, 2013). The clay solid solution is one of the strengths of the KIRMAT code. It allows the code to reproduce, at least to first order, the complex coupling between the composition of clays and the water chemistry through cationic exchanges. This multicomponent solid solution also aims to reflect the impurity of the precipitating clays during low-temperature water-rock interactions (Tardy and Fritz, 1981; Fritz, 1985). The algorithm also includes feedback effects between mineral mass budgets, reactive surfaces, and bedrock porosity evolution (Ngo et al., 2014). The KIRMAT code has been used in long-term geochemical evolution of radioactive waste deposits (Marty et al., 2010; Ngo et al., 2014) and the geochemical modeling of alluvial groundwaters (Lucas et al., 2010) and surface waters (Chabaux et al., 2017; Lucas et al., 2017).

5-2-Modeling strategy

The modeling approach developed in this work has been adapted from previous hydrochemical studies performed in the Vosges massif and the Rhine graben (Schaffhauser, 2013; Lucas et al., 2010; 2017). Based on the analyses of major elements and Sr-U isotopes, the recent work undertaken in the Strengbach and in the neighboring Ringelbach watersheds suggests that, in these granitic catchments, the springs are supplied by waters with relatively independent water pathways (Schaffhauser et al., 2014; Chabaux et al., 2017). In this context, the geochemical compositions of the spring waters have been simulated by considering a simple geometry, i.e., the granitic bedrock has been discretized along the main slopes with a 1D succession of cells. The chemical and conservative transport equations were solved simultaneously using these cells. A schematic representation of the modeling strategy is presented in Figure 5. This modeling approach assumes that there is no influence of deeper or lateral flow lines, which may induce a mixing with older waters. The length of the water pathway used to model the water chemistry of each spring has been estimated by taking the distance between the summit of the appropriate hillside and the emergence point of each spring. The calculated lengths of the water pathways obtained using this procedure are likely to be minimum estimates, as the tortuosity of the medium is not accounted for.

This modeling scheme also requires us to define the input and the output solutions; the latter obviously corresponds to the spring waters to be modeled. For the input solutions, and as the KIRMAT code is not designed to take into account the effect of the vegetation within the upper soil layers, it is not possible to directly use the rainwater as the input solution. The alternative approach proposed in this study is to consider the soil solutions collected at the greatest depths as the input solutions, because these soil solutions integrate the surface

processes that occur before the water percolates through the bedrock. Two of the deepest soil solution locations, HP-70 and VP-60 from the beech and the spruce sites, which are located on the southern and the northern parts of the watershed, respectively (data from Prunier et al., 2015), were used in this study as input solutions. The soil solutions measured at these sites exhibit a significant increase in mean annual pH (from 4.7 to 5.2 and from 4.4 to 4.8 for HP-70 and VP-60) and a strong decrease (by a factor of 10) in the Ca concentrations between 1990 and 2010 (Figures EA4, EA5, and EA6; Prunier et al., 2015).

The hydrochemical modeling of the spring waters also requires estimation of the bedrock porosity, the thermodynamic and kinetic constants describing mineral dissolution, and the reactive surfaces of the minerals. Bedrock porosity has been determined by imbibition experiments and is 3±0.5 % for the HPT facies and 6.8±1.2 % for the CA facies (El Gh'Mari, 1995). The thermodynamic and kinetic constants for the primary mineral dissolution reactions and the associated references are given in Electronic Annex in Table EA1 and Table EA2. A constant temperature of 6°C, which corresponds to the mean annual temperature of the spring waters (OHGE data), has been used for all the simulations. The thermodynamic constants at 6°C have been determined by a polynomial interpolation of the existing constants, and the kinetic constants at 6°C have been recalculated from the activation energy of the dissolution reactions (Table EA2). The partial pressure of CO_2 is considered to be higher than the atmospheric partial pressure, as it is commonly measured in the underground medium, and it is set to a constant and typical value of 2.5×10^{-3} atm (Hinkle, 1994; Bouma et al., 1997). For the estimation of the reactive surfaces, a spherical geometry is assumed for all the minerals present in the bedrock. The mean sizes of the different primary minerals are estimated from macroscopic descriptions and observations of thin

sections of the bedrock samples. The reactive surface Sp (m^2 / kg H_2O) for a given primary mineral is thus calculated by:

$$Sp = Vp * \frac{S}{V} \quad (2)$$

where Vp is the volume of mineral per kg of H_2O (cm^3 / kg H_2O), and S and V are the surface and the volume of the sphere representative of the considered mineral (μm^2 and μm^3). The volume Vp is obtained by:

$$Vp = X * \frac{(1-w) * \frac{1000}{\rho}}{w} \quad (3)$$

where w is the bedrock porosity, ρ is the water density (g/cm^3), and X is the volumetric fraction of the considered mineral. The mineral volumetric fractions and the calculated specific surfaces for the HPT and CA facies are given in Table 1. The mineral apatite is an exception to this rule. It is characterized by a low abundance and a small grain size. Thus, its reactive surface cannot be estimated from observations of mineral size, and it has been adjusted to generate solute Ca^{2+} concentrations having the same order of magnitude as the spring concentrations measured in 1990. For the clay minerals, the choice of the different clay solid solution end members is based on mineralogical analyses performed in previous studies using X-ray diffraction, which indicate that illite and montmorillonite/smectite are the dominant clay minerals in the granite of the Strengbach watershed (Fichter et al., 1998; Ackerer et al., 2016). The thermodynamic data used for the solid solution end members are presented in Table EA3. In addition to the clay solid solution, a small amount of illite is defined as a primary mineral to represent the background clay content acquired during the hydrothermal alteration of the granite (Table 1).

To model the CS springs, which drain the southern and weakly hydrothermally altered part of the watershed, the HPT facies has been used to describe the bedrock mineralogy (Figure 1, Table 1). The soil solutions from the beech site, which were sampled at a depth of 70 cm (HP-70), have been used as input solutions for these simulations. For the RH3 spring, which drains the northern and hydrothermally altered part of the watershed, the CA facies has been used to describe the bedrock mineralogy (Figure 1, Table 1). The soil solutions from the spruce site, which were sampled at a depth of 60 cm on the same hill slope (VP-60), have been used as input solutions. Considering the emerging point of the ARG spring, which is located downward and in the vicinity of the Strengbach stream, whether the water is coming from the southern or the northern part of the watershed is not obvious, and these two hypotheses have been tested in the following.

5-3-Modeling of the spatial variability of the spring water chemistry

To assess the factors that control the spatial variability of the spring water chemistry, the modeling strategy presented in section 5-2 has been applied to simulate the mean chemical composition of the springs in 1990. To carry out this task, a first set of runs covering 10 years has been performed that employs the mean chemistry of the soil solutions measured in 1992-1993 as input solutions. The Darcy rate of each spring was adjusted to obtain the best match between the simulated and the measured pH values and dissolved concentrations. The adjusted Darcy rates are in accordance with the hydrodynamic parameters obtained from a 3D hydrogeological model of the Strengbach catchment (Beaulieu et al., 2016).

For the four CS springs that drain the weakly hydrothermally altered slopes, the KIRMAT model is able to capture the cations and the dissolved silica concentrations in 1990 (Figure 6). Moreover, the simulated pH values range from 6.23 to 6.41, and these values are in good

agreement with the field measurements, which range from 5.99 to 6.33. The results therefore indicate that it is possible to account for the slight chemical differences between the CS springs by only considering the differences in hydrological conditions: the modeling has been performed with a single bedrock facies (HPT) and the same input soil solution (HP-70), but the specific length of the water pathway and the water discharge varies among the springs. In this modeling context, the Ca^{2+} in solution is essentially derived from the dissolution of apatite present in the HPT facies (ranging from 4.2×10^{-5} to 2×10^{-5} mol/yr/kg H_2O and providing 90-95% of the Ca) and secondarily due to the dissolution of anorthite ($\approx 1.1 \times 10^{-5}$ mol/yr/kg H_2O, providing about 5-10% of the Ca). The importance of the apatite dissolution in the Ca budget of the spring waters is in accordance with the results of Sr-Nd isotopic investigations performed in the Strengbach catchment, which show independently that most of the Sr and Nd in the spring waters originates from the dissolution of apatite and lesser amounts of feldspar (see Aubert et al., 2001; Stille et al., 2009). The dissolution of the albite ($\approx 1.3 \times 10^{-4}$ mol/yr/kg H_2O, providing 100% of the Na), K-feldspar ($\approx 1.3 \times 10^{-5}$ mol/yr/kg H_2O, providing 17% of the K) and biotite ($\approx 5.8 \times 10^{-5}$ mol/yr/kg H_2O, providing 83% of the K and 100% of the Mg) deliver the Na^+, K^+, and Mg^{2+} cations in solution. The H_4SiO_4 is essentially derived from the dissolution of biotite and feldspars (providing 34% and 66% of the Si respectively), as the spring waters are systematically supersaturated with respect to quartz and muscovite. The results also show that, at the end of the simulations and for each CS spring, the precipitated clay solid solution is dominated by the Ca-illite, Ca-montmorillonite and Mg-montmorillonite end members (Figure 7). For each CS spring, both primary mineral dissolution and clay precipitation rates are higher in the first part than at the end of the water pathway. Significant differences can be noted in the rates of clay precipitation and apatite dissolution (up to a factor of 2), and modest differences are noted

for the other primary minerals (<5%). The higher variability in the apatite dissolution rates is due to the fact that it is the only primary mineral out of those used in the simulations that is affected by changes in pH. Shifts from the acid to the neutral pH-domain occur for the apatite dissolution along the water pathways (Figure 8a, Table EA2). In the 1990 case, and for the CS1 spring, approximately the first half of the water pathway belongs to the acid domain, whereas the second half reflects the neutral pH-domain (Figure 8a). The modeling results indicate that the apatite dissolution rate can reach 4.2×10^{-5} mol/yr/kg H_2O under acidic conditions (pH≈4.8), while it does not exceed 2×10^{-5} mol/yr/kg H_2O under neutral conditions (pH>5.7). In addition, there is an important evolution of the relative end member fractions of clay solid solution along the water pathway. Ca-montmorillonite and Mg-montmorillonite dominate within the first part of the path (80 to 60 % from 0 to about 200 m), and Ca-illite dominates in the second part (30 to 70 % from about 200 to 400 m; Figure 7). The simulations also indicate that the shift from the dominance of Ca-montmorillonite to the Ca-illite end member coincides approximately with the location of the transition in the pH domain for apatite dissolution, which suggests a strong coupling between the apatite and the clay mineral compositions along the water pathways.

To model the ARG spring, which is located in the vicinity of the Strengbach stream, the simulations show that the chemical composition of the ARG spring in 1990 can be easily reproduced if the water is considered to have come from the southern part of the watershed (HPT facies, Figure 9); however, the observations cannot be reproduced using the hydrothermally altered bedrock of the northern slope (CA facies). In addition, and by considering the HPT facies, the clay solid solution that precipitates during the simulation is similar to those obtained in the CS spring simulations. This hydrological function is supported by the similarity between the mean $^{87}Sr/^{86}Sr$ isotope ratio of the ARG spring (0.726680) and

437 those of the CS spring waters, especially the CS1 spring water (0.726677), whereas there are
438 substantial differences relative to the value of the RH3 spring waters (0.722363; Sr data in
439 Pierret et al., 2014).

440 For the RH3 spring waters, which drain from the northern part of the watershed (CA facies),
441 the simulated concentrations of Na^+, $Mg2^+$ and H_4SiO_4 in 1990 are much lower than the
442 measured concentrations (Figure 9). Furthermore, the Ca^{2+} concentration in solution is
443 clearly overestimated by a factor of two. The hydrothermally altered CA facies, which is used
444 as the reference bedrock in the modeling of the RH3 spring, is mainly composed of quartz,
445 muscovite and K-feldspar, but it is lacking in biotite and plagioclase feldspar (Table 1). The
446 absence of these primary minerals is directly responsible for the lack of Na^+, Mg^{2+} and H_4SiO_4
447 in solution. The overestimation of Ca^{2+} is driven by the lower clay precipitation rate in this
448 configuration. This reduced rate results from the lower rate of silica release from the
449 dissolution of primary minerals. In this case, the divergence between the simulated and
450 measured parameters indicates that the hydrothermally altered CA facies is not effective in
451 reproducing the chemistry of the RH3 spring. One of the reasons that could be proposed to
452 explain this discrepancy is that the CA facies may not be representative of the bedrock of the
453 whole hillslope drained by the RH3 spring. In fact, total disappearance of biotite and
454 plagioclase feldspar corresponds to the highest degree of hydrothermal alteration, which is
455 probably only locally achieved within the northern part of the watershed. By moderating the
456 degree of hydrothermal alteration of the CA facies and testing the possibility that small
457 amounts of plagioclase feldspar (7%) and biotite (2%) are still present in the bedrock (the
458 modified facies is indicated as CA* in Table 1), the simulated chemical properties are more
459 consistent with the field data (Figure 9). This test likely indicates that less hydrothermally
460 altered regions of the bedrock and/or some uncharacterized hydrothermal minerals might

play an important role in the acquisition of the RH3 spring chemistry. Further modeling of the spring waters draining the northern part of the watershed likely requires a better mineralogical description of the bedrock of the northern slope to correctly model the geochemical composition of the RH3 spring waters.

5-4-Response of the CS and ARG springs to modification of the soil solution chemistry

Given the results of the modeling of the spatial variability, the modeling of the temporal evolution has focused on the CS and the ARG springs, which are located within the southern part of the watershed, where the chemical composition of the spring water in 1990 has been correctly modeled. To simulate the response induced by a modification of the soil solution composition on the spring water chemistry, a second set of simulations has been performed with the soil solution measured in 2010 as the input solution to the system obtained from the previous simulations for 1990. The bedrock mineralogical properties at the end of the simulations in 1990, including the precipitated clay fractions, have been used to define the initial state for these new simulations. The hydrological parameters, such as the rates of water flow and the lengths of the flow paths, were assumed to remain unchanged between 1990 and 2010. This assumption is supported by the absence of significant trends in the mean annual water discharges of the different springs during this period (OHGE data, Viville et al., 2012). The simulations performed with this approach, which implies an abrupt change in the soil solution chemistry, is more schematic than the reality, as the soil solutions have also varied within the studied period. However, the geochemical variations in the soil solution compositions are not monotonic from 1990 to 2010. For instance, the time evolution of the chemical compositions of the soil solution HP-70 within the beech plot is rather smooth from 1993 and 1998 and much larger after 2003, especially in terms of pH

484 and the Ca^{2+}, K^{+} and Mg^{2+} concentrations (Prunier et al., 2015; Figure EA4, EA5, EA6). Thus,
485 even if the simulations cannot precisely reproduce the temporal evolution of the spring
486 chemistry between 1990 and 2010, they should give a relatively realistic indication of the
487 mechanisms involved in the response of the spring water chemistry to a modification of the
488 incoming soil solution compositions, as well as the time required for the system to reach a
489 new equilibrium state.

490 A first important result of the above modeling approach is to show that a new equilibrium
491 state is reached relatively quickly, i.e., in less than 5 years after the modification of the soil
492 solution chemistry. The simulations also indicate that the dissolution rates of biotite and
493 feldspar decrease only slightly between the two periods, explaining relative stability of the
494 K^{+}, $Mg^{2+,}$ Na^{+} and H_4SiO_4 concentrations during the studied period. On the other hand, the
495 modifications induced by the pH increase and the Ca^{2+} concentration decrease in the soil
496 solutions significantly affect the behaviors of apatite and the clay minerals. As the pH of the
497 soil solutions increase significantly between 1990 and 2010 (from about 4.7 to 5.2 for HP-
498 70), the lengths of the water pathways characterized by rapid dissolution of apatite are
499 shorter in 2010, while the neutral domains of apatite dissolution are longer (Figure 8b). As a
500 result, for the CS1 spring, the average apatite dissolution rate along the water pathways
501 decreases by approximately 20% between 1990 and 2010. For the clay minerals, it is not the
502 precipitation rate of the clay solid solution which is modified; instead, the composition of the
503 precipitated clay solid solution changes significantly from 1990 to 2010 (Figure 7). Based on
504 the simulation results, the increase in pH and the decrease in Ca^{2+} concentrations in the soil
505 solutions produce lower proportions of Ca-montmorillonite and Mg-montmorillonite in the
506 first part of the water path (30 % from 0 to 80 m) and a larger amount of Ca-illite in the
507 second part (30 to 80 % from 80 to 400 m; Figure 7). As in the 1990 case, the shift between

508 the dominance of the Ca-montmorillonite end member to that of the Ca-illite end member
509 corresponds approximately to the shift in the pH-domain related to apatite dissolution. Such
510 an evolution of the composition of the clay solid solution implies that the Ca content of the
511 clay minerals increases by 10% for the CS1 spring between 1990 and 2010. The modeling
512 results thus indicate that modifications to the soil solution chemistry impact both the apatite
513 dissolution rates and the incorporation of Ca in the clay mineral structures, which
514 progressively modifies the chemical composition of the water along its path within the
515 bedrock.

516 When comparing the chemical trends along a water pathway after a perturbation with an
517 unperturbed system, it is interesting to note that both cases will lead to the same final
518 steady state concentration. For the Strengbach case, such a steady state is achieved after the
519 water has traversed a relatively long pathway within the bedrock, much longer than the
520 lengths of the water pathways assumed for the simulations of the different springs. This is
521 why the variations in the incoming soil solutions have a substantial impact on the emerging
522 spring waters. However, the water/rock interactions highlighted in the previous simulations
523 progressively dampen the perturbations induced by the soil solution changes. Because the
524 chemical compositions of the CS and the ARG springs have been modeled with the same
525 bedrock facies, the attenuation of the perturbation is a function only of the mean water
526 residence time, which is controlled by the length of flow path and the discharge of the
527 springs. For the CS1 spring, which is characterized by a shorter water residence time, the soil
528 solution changes have an important impact on both the apatite dissolution and the
529 composition of the clays, leading to a strong decrease in the simulated Ca^{2+} concentrations
530 between 1990 and 2010. For the other CS springs and the ARG spring, the same mechanisms
531 are involved in the decrease in the Ca^{2+} concentrations, but the magnitude of the decrease is

532 shaped by the different hydrological conditions and water pathways (Figure 10). For
533 example, the CS2, CS4 and ARG springs, which emerge at a lower altitude than the CS1
534 spring, exhibit a smaller decrease in the Ca^{2+} concentrations, as the longer water pathways of
535 these springs moderate the impact of the soil solution changes. For the CS3 spring, it is the
536 lower water flow rate of this spring which dampens the variations in the soil solutions by
537 increasing the water/rock interaction time.

538 In this context, the simulated concentrations show that the KIRMAT code captures the
539 particular chemical evolution of the CS springs from 1990 to 2010, i.e., the significant
540 decrease in Ca^{2+} and the relative stability or the slight decrease in dissolved silica and the
541 other cations (Figure 11). A test simulation has been performed in which the precipitation of
542 clay minerals in the granitic bedrock has been prevented. Without any clay precipitation, the
543 test simulation indicates that the pH of the spring water stabilizes rapidly along the water
544 pathways and above the pH of the apatite neutral domain (pH>6). In this extreme case, the
545 apatite dissolution rate varies less over the studied period, and the model is not able to
546 reproduce the decrease in Ca^{2+} between 1990 and 2010. Together, these modeling results
547 show (1) that the decrease in Ca^{2+} in the spring water is explained by the evolution of the soil
548 solution chemistry and the interactions between the apatite and the clay minerals, and (2)
549 the relative stability of the other cations and the dissolved silica is due to the weak variations
550 in the dissolution rates of other primary minerals and the stability of the bulk precipitation
551 rates of the clay minerals.

552 The modeling results obtained in this study therefore support the views that clay minerals
553 should not be considered as inert products of weathering processes and that the
554 precipitation of clays, which impact spring water chemistry, is also a factor that controls the

555 dissolution rates of primary minerals. Such interactions between the primary and the
556 secondary minerals are in accordance with the results from previous studies that involve
557 numerical modeling of soil profile development (Maher et al., 2009) or the chemistry of soil
558 solutions in the Strengbach catchment (Goddéris et al., 2006). At the same time, the results
559 obtained in this study show that the temporal evolution of the spring chemistry cannot be
560 explained solely by variations in clay mineral compositions, i.e., simple modifications of the
561 chemical composition of the precipitated clays or the ionic exchange capacity of the clay
562 minerals. Instead, the interrelations between the changes in the apatite dissolution rate and
563 the clay mineral compositions are definitely involved.

564 **6-Discussion and geochemical implications**

565 **6-1-Spatial and temporal uniformity of the weathering fluxes**

566 In addition to the modeling of the water-rock interactions along the flow path in the aquifer,
567 monitoring the geochemical composition and discharge of the Strengbach springs allows to
568 discuss the variability of the chemical fluxes exported by the different springs during the
569 1986-2010 period. The results show an almost perfect correlation between the calculated
570 chemical fluxes and the water discharges for all the Strengbach springs (Figure 12). The data
571 also highlight that even if the substratum includes slight lithological variations, the chemical
572 fluxes exported for a given water discharge are highly comparable from one spring to
573 another (Figure 12). This observation likely means that the nature of the primary minerals
574 and the weathering phases involved in the water-rock interactions controlling the chemical
575 fluxes exported by the different springs must be relatively similar within the Strengbach
576 catchment. This interpretation can certainly be extended to the other catchments exhibiting
577 weak lithological variations and relatively stable chemical compositions for several spring or

stream waters. This conclusion is also consistent with modeling results, which show that the chemical compositions of the CS and ARG springs can be correctly described using the same mineralogical assemblages. For the RH3 spring, which is located within the northern part of the catchment, the inability of the model to precisely capture the chemical composition of this spring complicates the explanation of the comparable exported fluxes. At this stage, and based on the similarity of the exported fluxes from the springs between the two parts of the watershed, it might be proposed that the lithological variations within the catchment have a relatively limited impact on the nature of the weathering reactions controlling the solute concentrations of H_4SiO_4 and Na^+, which are the two dominant chemical species of the dissolved loads carried by the Strengbach springs. As it is also apparent from the chemical evolution of the spring waters, the only chemical fluxes that vary significantly with time and from one spring to another are the Ca^{2+} fluxes. However, because the contribution of Ca^{2+} to the total weathering fluxes is modest (<10%), and due to the relative stability of the concentrations of dissolved silica and other cations, the global weathering fluxes exported by the springs remain relatively stable over the studied period. Thus, even if the watershed has been affected by recent perturbations that are reflected in the chemistry of the soil solutions (Prunier et al., 2015), and that have affected the Ca^{2+} concentrations and fluxes of the spring waters (this study), the total chemical fluxes carried by the springs have only varied slightly from 1990 to 2010. The absence of extensive anthropization, pesticide, and agricultural spreading within the Strengbach watershed may also explain this stability.

6-2 Chemostatic behavior of the Strengbach springs

The relative stability of the chemical concentrations over a wide range of water discharge is not unique to the Strengbach catchment. This “near-chemostatic” behavior has been

601 described in other experimental catchments where the exported fluxes are nearly
602 proportional to the water discharges (Godsey et al., 2009; Clow and Mast, 2010; Thompson
603 et al., 2011). Different mechanisms have been hypothesized to explain the stability of the
604 solute concentrations in natural waters. For instance, based on the observation that mineral
605 weathering rates are directly dependent on reactive mineral surfaces (Lasaga et al., 1994), it
606 has been proposed that the relationship between concentrations and discharges may result
607 from a change in the reactive mineral surface area in response to changing hydrologic
608 conditions (Godsey et al., 2009; Clow and Mast, 2010). Among different scenarios, vertical
609 expansion of the saturated zone and hence an increase in the reactive mineral surface areas
610 in contact with groundwater might be envisaged during snowmelt or rainfall events. On the
611 other hand, during drought events associated with low discharge periods, the reactive
612 mineral surface area would decrease (Clow and Mast, 2010). Alternatively, the chemostatic
613 behavior of small catchments has been interpreted by considering that the fluid residence
614 time in the watersheds is long enough for the stream to reach an equilibrium concentration,
615 which means, that the length scale of the water pathway in the catchments is longer than
616 the distance required for the fluid to reach a chemical equilibrium between dissolution of
617 primary minerals and precipitation of secondary minerals (Maher, 2010; 2011).

618 The numerical approach developed in this work allows characterization of the evolution of
619 the water chemical composition along the flow paths. Therefore, the relevance of the above
620 scenarios in explaining the chemostatic behavior of the Strengbach springs can be discussed.
621 The simulation results show unambiguously that the pathway length needed to reach an
622 equilibrium concentration is much longer than those estimated within the catchment for the
623 different springs. As an illustration, based on the simulations of the CS1 spring waters, a
624 distance as long as 15-20 km is required for the water to reach an equilibrium concentration

625 of approximately 1.7×10^{-3} mol/L for Ca^{2+} (Figure 10), and of about 1.9×10^{-3} mol/L for
626 H_4SiO_4 (not shown). Taken as such, these results imply that the chemostatic behavior of the
627 Strengbach springs cannot be explained by the mobilization of waters close to a chemical
628 equilibrium state. Other scenarios must be invoked, such as an hydrological control implying
629 a relative similarity of the water residence times feeding individual springs, regardless of
630 discharge. Large water storage within the substratum, which can be envisaged for the
631 Strengbach catchment (Viville et al., 2006), associated with rapid hydrological response of
632 the aquifer to rainwater inputs may account for such a behavior. The hydrological
633 interpretation for the Strengbach chemostatic behavior is reinforced by the consistency
634 between some modeling results and field data. Firstly, the amount of precipitated clay is
635 realistic compared to field observations. A test simulation performed over approximately 20
636 kyr produced a mass fraction of clay minerals of 2-3% in the first part of the water pathway
637 of the CS1 spring. The duration of 20 kyr corresponds approximately to the recent
638 weathering stage of the granitic bedrock since the last glacial maximum (Ackerer et al.,
639 2016). This is consistent with the fraction of ≈2% of clay minerals determined by X-ray
640 diffraction analysis in the granitic basement of the weathering profiles located within the
641 southern part of the Strengbach catchment (Fichter et al., 1998; Ackerer et al., 2016).
642 Secondly, in our modeling work, the end members of the clay solid solution are relevant and
643 have been selected on the basis of X-ray diffraction analyses of bedrock samples collected in
644 the field (Fichter et al., 1998; Ackerer et al., 2016). A different choice of the precipitating clay
645 minerals would modify both the chemical compositions and the chemical equilibrium lengths
646 of the spring waters. For example, a test simulation that only considers that small amount of
647 kaolinite is precipitating, as in Maher (2009, 2010), shows that an equilibrium concentration
648 for H_4SiO_4 is achieved within only about 300 m along the water pathways (not shown). In the

649 extreme case, in which clay precipitation is totally prevented, the equilibrium concentration
650 would be achieved in less than 200 m along the water pathways. Nevertheless, these two
651 theoretical cases are not able to capture the chemical evolution of the springs between 1990
652 and 2010, in contrast to the simulations made with the secondary clay mineral assemblages
653 retained in our study. Thus, at this stage, the only parameters that may impact our
654 interpretation for the chemostatic behavior of the Strengbach springs are the values
655 employed for the kinetic constants of the primary mineral dissolution reactions. For all of the
656 simulations, the kinetic constants of the primary mineral dissolution reactions are those
657 determined through laboratory experiments (Table EA2), following procedures used in other
658 modeling studies (e.g., Goddéris et al., 2006). Such experimental values may overestimate
659 field values (White and Brantley, 2003). Different possibilities have been proposed to explain
660 the apparent discrepancy between experimental and field data, such as, for instance, a
661 physical occlusion of the primary minerals by secondary phases (White and Brantley, 2003)
662 or the development of amorphous silica-rich layers on the mineral surfaces (Daval et al.,
663 2011; Wild et al., 2016). Accordingly, some modeling studies have adjusted and decreased
664 the kinetic constants of the primary mineral dissolution reactions (e.g., Maher, 2009; 2010;
665 Lucas et al., 2017). Adjusting kinetic constants will result in different dissolution rates of the
666 primary minerals, and thus in different chemical equilibrium lengths of the spring waters.
667 However, in the Strengbach case, the ability of the simulations to capture the spatial
668 variability and the time evolution of the spring water chemistry do not encourages us to
669 modify the kinetic constants used for the simulations. Hence, our results suggest that the
670 chemostatic behavior of the Strengbach springs is explained by an hydrological control of the
671 water residence times feeding individual springs, rather than a scenario assuming chemical
672 equilibrium state. We are nevertheless fully aware that the definitive choice between these

673 different schemes, whatever the considered catchments, will be based on our future ability
674 to correctly estimate the kinetic constants of dissolution of primary minerals and
675 precipitation of secondary minerals in the natural environment.

676 **6-3-Comparison of current and long-term weathering rates**

677 The calculation of the weathering fluxes exported by the springs enables comparison of the
678 current weathering rates with the long-term ones determined along a regolith profile
679 located on the summit of the southern part of the catchment (Ackerer et al., 2016). This
680 profile is located on the same slope as the CS springs and integrates the chemical losses
681 associated with regolith formation over the last 20 kyr (Ackerer et al., 2016). The calculated
682 current and long-term weathering rates are given in the Table 2. The results indicate that,
683 whatever parameter values are used for the atmospheric correction, there is a good
684 consistency between the current H_4SiO_4 weathering fluxes estimated for the four CS springs
685 and the long-term ones (approximately 2-3 T/km²/yr). These estimates are also quite
686 consistent with the current fluxes of 2.89 T/km²/yr for H_4SiO_4 determined at the watershed
687 scale in the Strengbach stream (Viville et al., 2012). Given the uncertainty and the
688 assumptions made in performing the atmospheric contribution corrections, the data also
689 suggest a good agreement between the current and the long-term weathering fluxes of Na^+.
690 On the other hand, for Mg^{2+}, Ca^{2+} and K^+, the current weathering fluxes determined for the
691 springs and the stream waters are different from the long-term estimates. Substantially
692 higher current rates are obtained for Ca^{2+}, slightly higher ones are obtained for Mg^{2+} and
693 lower ones are obtained for K^+ (Table 2). For Ca^{2+}, the difference between the long-term and
694 the current estimates ranges from a factor of 4 to 18, as both the long-term estimates and
695 the current atmospheric corrections contain substantial uncertainties.

696 The modeling approach presented in this work can be used to discuss the origins of such
697 differences. By only considering a modification of the two main parameters that are involved
698 in explaining the 20-year variations, namely the modification of the pH and the
699 concentrations of Ca^{2+} in the soil solutions, the modeling results demonstrate that it is not
700 possible to explain the observed decreases in the fluxes of Ca^{2+} exported by the different
701 springs. A 4 to 18-fold difference between the long-term and the current weathering fluxes
702 for Ca^{2+} thus requires a modification of the other bio-climatic parameters of the weathering
703 system, especially the water temperature, the partial pressure of CO_2 (pCO_2) and the water
704 flows. To reproduce in a schematic manner the climatic conditions that are thought to have
705 prevailed in the watershed before the warming associated with the onset of the Holocene, a
706 simulation has been performed in which a cooling from 6°C to 1°C for the spring water
707 temperatures, a higher pH of 5.7 for the soil solutions, and a lower partial pressure of CO_2
708 that corresponds to a pre-anthropogenic atmospheric level (200 ppmv) are considered. Such
709 pH and pCO_2 values for the deeper soil solutions and the percolating bedrock waters are
710 those expected for a system without any biological activity in the soil, which is clearly an
711 extreme situation. Under such conditions, the apatite weathering rate decreases in response
712 to the lower temperature and pCO_2 values, and the simulated Ca^{2+} concentrations are
713 approximately divided by a factor of 4 in the spring waters with respect to 1990 (Figure 13).
714 Because drier conditions prevailed during the last glacial maximum in central Europe
715 (Sirocko et al., 2016), lower water flows likely prevailed in the Strengbach watershed in the
716 past, which would decrease the exported fluxes of Ca^{2+} even further and explain the 4 to 18-
717 fold differences. Interestingly, the simulated H_4SiO_4 and Na^+ concentrations are less sensitive
718 to the temperature and the pCO_2 changes than the Ca^{2+} concentrations, and they only vary
719 by 20% between the simulations representing past and current conditions. These findings

720 are also in accordance with the geochemical dataset and the 1990-2010 modeling results,
721 which show that the Ca^{2+} concentrations in the Strengbach spring waters are much more
722 strongly affected by the recent superficial perturbations than the H_4SiO_4 and the Na^+
723 concentrations over decadal timescales. Taken together, these different results suggest that,
724 in a granitic catchment such as the Strengbach watershed, the silicate weathering processes
725 are little affected by environmental changes, both at the millennial time scale of Quaternary
726 climatic changes and at the multi-annual scale of recent environmental changes. Only
727 chemical elements such as Ca^{2+}, for which the budget in the spring waters is controlled by
728 the behavior of the clays and of minor minerals such as apatite, and elements such as K^+,
729 which are strongly affected by the dynamics of the biological processes, are significantly
730 impacted by the environmental changes.

731 **Conclusion**

732 This study highlights the potential of combining monitoring data and the hydrochemical
733 modeling of surface waters to investigate the variability of the weathering processes within
734 a small watershed. The KIRMAT simulations demonstrate that the significant decrease in the
735 Ca^{2+} concentrations in the spring waters is a reflection of both the dissolution rate variability
736 of the apatite mineral and the changes in clay composition in response to the evolution of
737 the input soil solution. The results also indicate that the magnitude of the changes in Ca^{2+}
738 concentrations is shaped by the different hydrological conditions and the specific water
739 residence time of each spring. Apart from the important pH and Ca^{2+} concentration changes,
740 the simulations also account for the weak variability in the Na^+ and the H_4SiO_4 concentrations
741 and explain the relative stability of the global weathering fluxes exported by the springs
742 during the studied period. Our results furthermore suggest that the chemostatic behavior of

743 the Strengbach springs is explained by an hydrological control of the water residence times
744 feeding individual springs, rather than a scenario assuming chemical equilibrium state. This
745 conclusion for the Strengbach site, but also for any other hydrological contexts, depends on
746 our ability to correctly estimate the kinetic constants of both the primary mineral dissolution
747 and the clay mineral precipitation. Finally, the comparison between the current and the
748 long-term weathering rates determined from the spring water monitoring and along a
749 regolith profile shows that the modern chemical fluxes of Ca^{2+} are higher than the long-term
750 ones, while the relative stability of the silicate weathering processes is probably true over a
751 long time scale. These different results indicate that silicate weathering processes are
752 characterized by a weak spatial and temporal variability, whereas chemical species such as
753 Ca^{2+}, for which the budget in the spring waters is controlled by the behavior of the clays and
754 of minor minerals such as apatite, are significantly impacted by the current environmental
755 changes, as well as Quaternary climatic changes.

756 **Acknowledgements**: This work was supported by a Ph. D. scholarship awarded to J. Ackerer
757 by the Region Alsace, France and the BRGM, Orléans, France. It was financially supported by
758 funding from the CPER-Alsace REALISE program, and by the French ANR Program under
759 grant agreement ANR-15-CE06-0014 (Projet CANTARE- Alsace) and grant agreement ANR-15-
760 CExxx. Yves Godderis is warmly thanked for very constructive and positive comments on a
761 preliminary version of this work, which also benefited from fruitful discussions with P. Stille
762 and J. van der Woerd. This is a LHyGeS-EOST contribution.

Figure captions

Figure 1: sampling locations within the Strengbach catchment. Stars, circles, diamonds and triangles represent the springs, the soil solutions, the bedrock facies and the weathering profiles respectively.

Figure 2: (a) spatial variability of the Ca^{2+} and Mg^{2+} concentrations for the different springs emerging in the Strengbach catchment (b) seasonal variability and decadal evolution of the Ca^{2+} and the H_4SiO_4 concentrations for spring CS1 between 1990 and 2012.

Figure 3: temporal evolution of the concentrations of cations (Na^+, K^+, Ca^{2+}, Mg^{2+}), anions (SO_4^{2-}, NO_3^-, Cl^-) and dissolved silica (H_4SiO_4) measured at the CR spring collector from 1990 to 2010.

Figure 4: temporal evolution of the concentrations of cations (Na^+, K^+, Ca^{2+}, Mg^{2+}) and dissolved silica (H_4SiO_4) for the different CS, ARG and RH3 springs from 1990 to 2010.

Figure 5: conceptual scheme used in the modeling. The granitic bedrock is discretized into a 1D succession of cells along the water path, and soil solutions are used as input solutions. For a given cell M, the concentration variation ΔCe for an element e is calculated from geochemical and transport fluxes. The output solutions produced by the system are considered to represent the spring waters that are to be modeled.

Figure 6: simulation of the CS springs in 1990 with the HPT facies. Blue and red bars represent the modeled and the measured elemental concentrations of the CS springs. Gray bars represent the measured concentrations of the soil solution HP-70 in 1992.

Figure 7: relative fractions of the different end members of the clay solid solution along the water pathway. The results are presented for the CS1 spring in 1990 (a) and in 2010 (b).

Figure 8: evolution of the simulated pH along the water pathway for the CS1 spring in 1990 and 2010. The modeling results allow identification of two distinct zones: (1) a zone with pH<6 that is characterized by rapid apatite dissolution and the dominance of Ca-montmorillonite and (2) a zone with pH>6 that is characterized by slower apatite dissolution and the dominance of Ca-illite.

Figure 9: simulation of the ARG spring in 1994 and 2008 with the HPT facies and the RH3 spring in 1990 with the CA and the CA* facies. Blue and red bars represent the modeled and the measured elemental concentrations of the spring waters. Gray bars represent the measured concentrations of the soil solution HP-70 for the simulation of ARG and the measured concentrations of the soil solution VP-60 for the simulation of RH3.

Figure 10: evolution of the simulated Ca^{2+} concentrations along the water pathways for the CS1 and CS2 springs in 1990 and 2010. The different water residence times imply different responses of the Ca^{2+} concentrations to changes in the soil solution. The CS3 and CS4 springs are not represented in this figure for reasons of clarity, but the same mechanisms are involved. The results are also shown for the CS1 spring in 1990 and 2010 along a theoretical water pathway of 20 km.

Figure 11: simulation of the CS springs in 2010 with the HPT facies. Blue and red bars represent the modeled and the measured elemental concentrations of the CS springs. Gray bars represent the measured concentrations of the soil solution HP-70 in 2010.

Figure 12: chemical weathering fluxes of cations (Na^+, K^+, Ca^{2+}, Mg^{2+}) and dissolved silica for the different springs from 1990 to 2010.

Figure 13: evolution of the simulated Ca^{2+} concentrations along the water pathways for the CS1 spring in the recent periods and in the 20 000 years before the present day. The domain of the concentrations corresponding to the long-term estimates is represented by the black rectangle.

Table captions

Table 1: mineralogical compositions and reactive surfaces for the different bedrock facies used in this study (i.e., the HPT, CA and CA* facies).

Table 2: Estimated chemical fluxes for the different CS springs (1990-2010) and for the studied regolith profile. (F) uncorrected. (A) corrected for atmospheric deposition. (B) corrected for atmospheric deposition and tree harvesting. (C) corrected for atmospheric deposition and tree

811 growth. The corrections were calculated using the method presented in Viville et al., 2012. The
812 chemical species are not impacted in the same way by the different possible corrections because the
813 atmospheric contribution depends on how the elements are concentrated in the rainwater and is
814 affected by biomass cycling. As an example, these factors are much more important for K^+ than for
815 the dissolved silica (H_4SiO_4).

816 **References**

817 Ackerer, J., Chabaux, F., Van der Woerd, J., Viville, D., Pelt, E., Kali, E., ... & Négrel, P. (2016).
818 Regolith evolution on the millennial timescale from combined U–Th–Ra isotopes and
819 in situ cosmogenic 10 Be analysis in a weathering profile (Strengbach catchment,
820 France). *Earth and Planetary Science Letters*, *453*, 33-43.

821 Aubert, D., Stille, P., & Probst, A. (2001). REE fractionation during granite weathering and
822 removal by waters and suspended loads: Sr and Nd isotopic evidence. *Geochimica et*
823 *Cosmochimica Acta*, *65*(3), 387-406.

824 Beaulieu, E., Goddéris, Y., Labat, D., Roelandt, C., Oliva, P., & Guerrero, B. (2010). Impact of
825 atmospheric CO2 levels on continental silicate weathering. *Geochemistry,*
826 *Geophysics, Geosystems*, *11*(7).

827 Beaulieu, E., Goddéris, Y., Donnadieu, Y., Labat, D., & Roelandt, C. (2012). High sensitivity of
828 the continental-weathering carbon dioxide sink to future climate change. *Nature*
829 *Climate Change*, *2*(5), 346-349.

830 Beaulieu, E., Lucas, Y., Viville, D., Chabaux, F., Ackerer, P., Goddéris, Y., & Pierret, M. C.
831 (2016). Hydrological and vegetation response to climate change in a forested
832 mountainous catchment. *Modeling Earth Systems and Environment*, *2*(4), 191.

833 Bouma, T. J., Nielsen, K. L., Eissenstat, D. M., & Lynch, J. P. (1997). Soil CO2 concentration
834 does not affect growth or root respiration in bean or citrus. *Plant, Cell &*
835 *Environment*, *20*(12), 1495-1505.
836 Chabaux, F., Viville, D., Lucas, Y., Ackerer, J., Ranchoux, C., Bosia, C., ... & Lerouge, C. (2017).
837 Geochemical tracing and modeling of surface and deep water–rock interactions in
838 elementary granitic watersheds (Strengbach and Ringelbach CZOs, France). *Acta*
839 *Geochimica*, 36, 363–366.
840 Clow, D. W., & Mast, M. A. (2010). Mechanisms for chemostatic behavior in catchments:
841 implications for CO 2 consumption by mineral weathering. *Chemical Geology*, *269*(1),
842 40-51.
843 Dambrine, E., Pollier, B., Poszwa, A., Ranger, J., Probst, A., Viville, D., ... & Granier, A. (1998).
844 Evidence of current soil acidification in spruce stands in the Vosges Mountains, north-
845 eastern France. *Water, Air, and Soil Pollution*, *105*(1-2), 43-52.
846 Daval, D., Sissmann, O., Menguy, N., Saldi, G. D., Guyot, F., Martinez, I., ... & Hellmann, R.
847 (2011). Influence of amorphous silica layer formation on the dissolution rate of
848 olivine at 90 C and elevated pCO 2. *Chemical Geology*, *284*(1), 193-209.
849 Donnini, M., Frondini, F., Probst, J. L., Probst, A., Cardellini, C., Marchesini, I., & Guzzetti, F.
850 (2016). Chemical weathering and consumption of atmospheric carbon dioxide in the
851 Alpine region. *Global and Planetary Change*, *136*, 65-81.
852 Egli, M., Mirabella, A., & Sartori, G. (2008). The role of climate and vegetation in weathering
853 and clay mineral formation in late Quaternary soils of the Swiss and Italian Alps.
854 *Geomorphology*, *102*(3), 307-324.
855 El Gh'Mari, A. (1995). Étude pétrographique, minéralogique et géochimique de la dynamique
856 d'altération d'un granité soumis aux dépôts atmosphériques acides (bassin versant du

857 Strengbach, Vosges, France): mécanisme, bilan et modélisation, en dépôt à la Soc.
858 géol. *France ThèseUniversité Louis-Pasteur*, 200.
859 Eyring, H. (1935). The activated complex in chemical reactions. *The Journal of Chemical*
860 *Physics*, *3*(2), 107-115.
861 Fichter, J., Turpault, M. P., Dambrine, E., & Ranger, J. (1998). Mineral evolution of acid forest
862 soils in the Strengbach catchment (Vosges Mountains, NE France). *Geoderma*, *82*(4),
863 315-340.
864 Fritz, B. (1985). Multicomponent solid solutions for clay minerals and computer modeling of
865 weathering processes. In *The chemistry of weathering* (pp. 19-34). Springer
866 Netherlands.
867 Gangloff, S., Stille, P., Pierret, M. C., Weber, T., & Chabaux, F. (2014). Characterization and
868 evolution of dissolved organic matter in acidic forest soil and its impact on the
869 mobility of major and trace elements (case of the Strengbach watershed).
870 *Geochimica et Cosmochimica Acta*, *130*, 21-41.
871 Gérard, F. (1996). *Modélisation géochimique thermodynamique et cinétique avec prise en*
872 *compte des phénomènes de transport de masse en milieu poreux saturé* (Doctoral
873 dissertation).
874 Gérard, F., Clement, A., & Fritz, B. (1998). Numerical validation of a Eulerian hydrochemical
875 code using a 1D multisolute mass transport system involving heterogeneous
876 kinetically controlled reactions. *Journal of contaminant hydrology*, *30*(3), 201-216.
877 Goddéris, Y., François, L. M., Probst, A., Schott, J., Moncoulon, D., Labat, D., & Viville, D.
878 (2006). Modelling weathering processes at the catchment scale: The WITCH
879 numerical model. *Geochimica et Cosmochimica Acta*, *70*(5), 1128-1147.

880 Goddéris, Y., Roelandt, C., Schott, J., Pierret, M. C., & François, L. M. (2009). Towards an
881 integrated model of weathering, climate, and biospheric processes. *Reviews in*
882 *Mineralogy and Geochemistry*, *70*(1), 411-434.
883 Goddéris, Y., & Brantley, S. L. (2013). Earthcasting the future Critical Zone. *Elementa*, *1*.
884
885 Godsey, S. E., Kirchner, J. W., & Clow, D. W. (2009). Concentration–discharge relationships
886 reflect chemostatic characteristics of US catchments. *Hydrological Processes*, *23*(13),
887 1844-1864.
888 Hinkle, M. E. (1994). Environmental conditions affecting concentrations of He, CO2, O2 and
889 N2 in soil gases. *Applied Geochemistry*, *9*(1), 53-63.
890 Knight, D. H., Yavitt, J. B., & Joyce, G. D. (1991). Water and nitrogen outflow from lodgepole
891 pine forest after two levels of tree mortality. *Forest Ecology and Management*, *46*(3-
892 4), 215-225.
893 Lasaga, A. C., Soler, J. M., Ganor, J., Burch, T. E., & Nagy, K. L. (1994). Chemical weathering
894 rate laws and global geochemical cycles. *Geochimica et Cosmochimica Acta*, *58*(10),
895 2361-2386.
896 Lebedeva, M. I., Fletcher, R. C., & Brantley, S. L. (2010). A mathematical model for steady-
897 state regolith production at constant erosion rate. *Earth Surface Processes and*
898 *Landforms*, *35*(5), 508-524.
899 Li, D. D., Jacobson, A. D., & McInerney, D. J. (2014). A reactive-transport model for examining
900 tectonic and climatic controls on chemical weathering and atmospheric CO 2
901 consumption in granitic regolith. *Chemical Geology*, *365*, 30-42.
902 Lovett, G. M., Christenson, L. M., Groffman, P. M., Jones, C. G., Hart, J. E., & Mitchell, M. J.
903 (2002). Insect Defoliation and Nitrogen Cycling in Forests Laboratory, plot, and
904 watershed studies indicate that most of the nitrogen released from forest foliage as a

905 result of defoliation by insects is redistributed within the ecosystem, whereas only a
906 small fraction of nitrogen is lost by leaching. *BioScience*, *52*(4), 335-341.
907 Lucas, Y., Schmitt, A. D., Chabaux, F., Clément, A., Fritz, B., Elsass, P., & Durand, S. (2010).
908 Geochemical tracing and hydrogeochemical modelling of water–rock interactions
909 during salinization of alluvial groundwater (Upper Rhine Valley, France). *Applied*
910 *Geochemistry*, *25*(11), 1644-1663.
911 Lucas, Y., Chabaux, F., Schaffhauser, T., Fritz, B., Ambroise, B., Ackerer, J., & Clément, A.
912 (2017). Hydrogeochemical modeling (KIRMAT) of spring and deep borehole water
913 compositions in the small granitic Ringelbach catchment (Vosges Mountains, France).
914 *Applied Geochemistry*, *87*, 1-21.
915 Maher, K., Steefel, C. I., White, A. F., & Stonestrom, D. A. (2009). The role of reaction affinity
916 and secondary minerals in regulating chemical weathering rates at the Santa Cruz Soil
917 Chronosequence, California. *Geochimica et Cosmochimica Acta*, *73*(10), 2804-2831.
918 Maher, K. (2010). The dependence of chemical weathering rates on fluid residence time.
919 *Earth and Planetary Science Letters*, *294*(1), 101-110.
920 Maher, K. (2011). The role of fluid residence time and topographic scales in determining
921 chemical fluxes from landscapes. *Earth and Planetary Science Letters*, *312*(1), 48-58.
922 Marty, N. C., Fritz, B., Clément, A., & Michau, N. (2010). Modelling the long term alteration
923 of the engineered bentonite barrier in an underground radioactive waste repository.
924 *Applied Clay Science*, *47*(1), 82-90.
925 Murphy, W. M., & Helgeson, H. C. (1987). Thermodynamic and kinetic constraints on
926 reaction rates among minerals and aqueous solutions. III. Activated complexes and
927 the pH-dependence of the rates of feldspar, pyroxene, wollastonite, and olivine
928 hydrolysis. *Geochimica et Cosmochimica Acta*, *51*(12), 3137-3153.

Ngo, V. V., Delalande, M., Clément, A., Michau, N., & Fritz, B. (2014). Coupled transport-reaction modeling of the long-term interaction between iron, bentonite and Callovo-Oxfordian claystone in radioactive waste confinement systems. *Applied Clay Science*, *101*, 430-443.

Pierret, M. C., Stille, P., Prunier, J., Viville, D., & Chabaux, F. (2014). Chemical and U–Sr isotopic variations in stream and source waters of the Strengbach watershed (Vosges mountains, France). *Hydrology and Earth System Sciences*, *18*(10), 3969-3985.

Probst, A., Dambrine, E., Viville, D., & Fritz, B. (1990). Influence of acid atmospheric inputs on surface water chemistry and mineral fluxes in a declining spruce stand within a small granitic catchment (Vosges massif, France). *Journal of Hydrology*, *116*(1-4), 101-124.

Prunier, J. (2008). *Etude du fonctionnement d'un écosystème forestier en climat tempéré, par l'apport de la géochimie élémentaire et isotopique (Sr, U-Th-Ra): Cas du bassin versant du Strengbach (Vosges, France)* (Doctoral dissertation, Strasbourg 1).

Prunier, J., Chabaux, F., Stille, P., Gangloff, S., Pierret, M. C., Viville, D., & Aubert, A. (2015). Geochemical and isotopic (Sr, U) monitoring of soil solutions from the Strengbach catchment (Vosges mountains, France): Evidence for recent weathering evolution. *Chemical Geology*, *417*, 289-305.

Schaffhauser, T. (2013). *Traçage et modélisation des processus d'altération à l'échelle d'un petit bassin versant, le Ringelbach (Vosges, France)* (Doctoral dissertation, Strasbourg).

Schaffhauser, T., Chabaux, F., Ambroise, B., Lucas, Y., Stille, P., Reuschlé, T., ... & Fritz, B. (2014). Geochemical and isotopic (U, Sr) tracing of water pathways in the granitic Ringelbach catchment (Vosges Mountains, France). *Chemical Geology*, *374*, 117-127.

952 Sirocko, F., Knapp, H., Dreher, F., Förster, M. W., Albert, J., Brunck, H., ... & Röhner, M.
953 (2016). The ELSA-Vegetation-Stack: Reconstruction of Landscape Evolution Zones
954 (LEZ) from laminated Eifel maar sediments of the last 60,000 years. *Global and*
955 *Planetary Change*, *142*, 108-135.
956 Stille, P., Pierret, M. C., Steinmann, M., Chabaux, F., Boutin, R., Aubert, D., ... & Morvan, G.
957 (2009). Impact of atmospheric deposition, biogeochemical cycling and water–mineral
958 interaction on REE fractionation in acidic surface soils and soil water (the Strengbach
959 case). *Chemical Geology*, *264*(1), 173-186.
960 Tardy, Y., & Fritz, B. (1981). An ideal solid solution model for calculating solubility of clay
961 minerals. *Clay minerals*, *16*(3), 361-373.
962 Thompson, S. E., Basu, N. B., Lascurain, J., Aubeneau, A., & Rao, P. S. C. (2011). Relative
963 dominance of hydrologic versus biogeochemical factors on solute export across
964 impact gradients. *Water Resources Research*, *47*(10).
965 Viville, D., Chabaux, F., Stille, P., Pierret, M. C., & Gangloff, S. (2012). Erosion and weathering
966 fluxes in granitic basins: the example of the Strengbach catchment (Vosges massif,
967 eastern France). *Catena*, *92*, 122-129.
968 Viville D., Ladouche B., Bariac T. (2006). Isotope hydrological study of mean transit time in
969 the granitic Strengbach catchment (Vosges Massif, France). *Hydrol. Process.* 20, 1737-
970 1751. doi: 10.1002/hyp.5950.
971 White, A. F., & Brantley, S. L. (2003). The effect of time on the weathering of silicate
972 minerals: why do weathering rates differ in the laboratory and field?. *Chemical*
973 *Geology*, *202*(3), 479-506.
974 Wild, B., Daval, D., Guyot, F., Knauss, K. G., Pollet-Villard, M., & Imfeld, G. (2016). pH-
975 dependent control of feldspar dissolution rate by altered surface layers. *Chemical*
976 *Geology*, *442*, 148-159.

977 WRB, 2006. International Union Soil Sciences Working Group WRB. 2006. World reference
978 base for soil resources 2006. World Soil Resources Reports No. 103. FAO, Rome

979

980

981

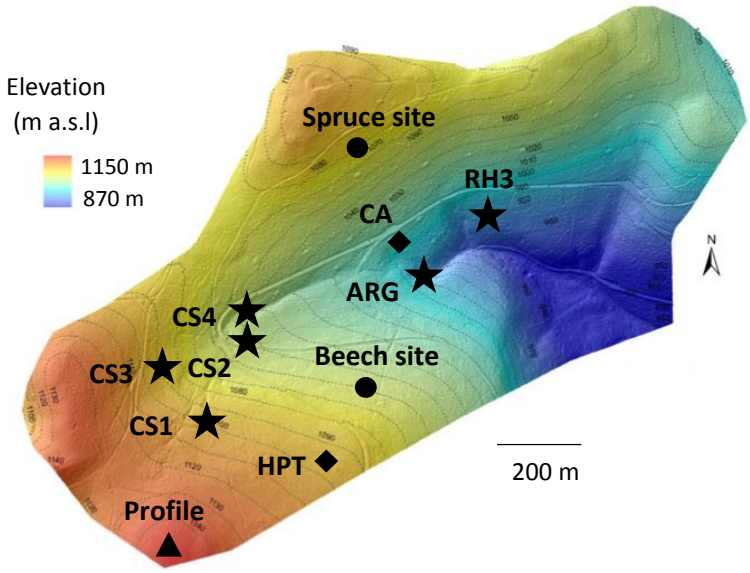
Elevation
(m a.s.l)
1150 m
870 m
Spruce site
RH3
CA
ARG
CS4
CS3
CS2
Beech site
CS1
HPT
Profile
N
200 m

Figure 1

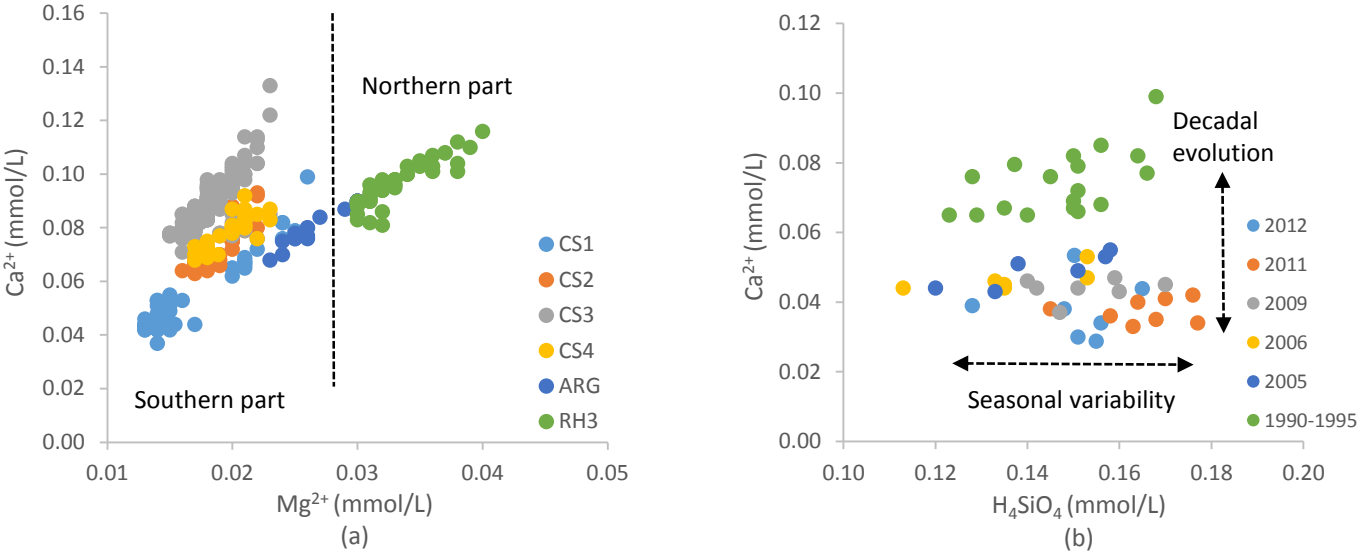
0.16
0.14
0.12
0.10
0.08
0.06
0.04
0.02
0.00
Ca2+ (mmol/L)
0.01
0.02
0.03
0.04
0.05
Mg2+ (mmol/L)
(a)
Northern part
Southern part
CS1
CS2
CS3
CS4
ARG
RH3
0.12
0.10
0.08
0.06
0.04
0.02
0.00
Ca2+ (mmol/L)
0.10
0.12
0.14
0.16
0.18
0.20
H4SiO4 (mmol/L)
(b)
Decadal evolution
Seasonal variability
2012
2011
2009
2006
2005
1990-1995

Figure 2

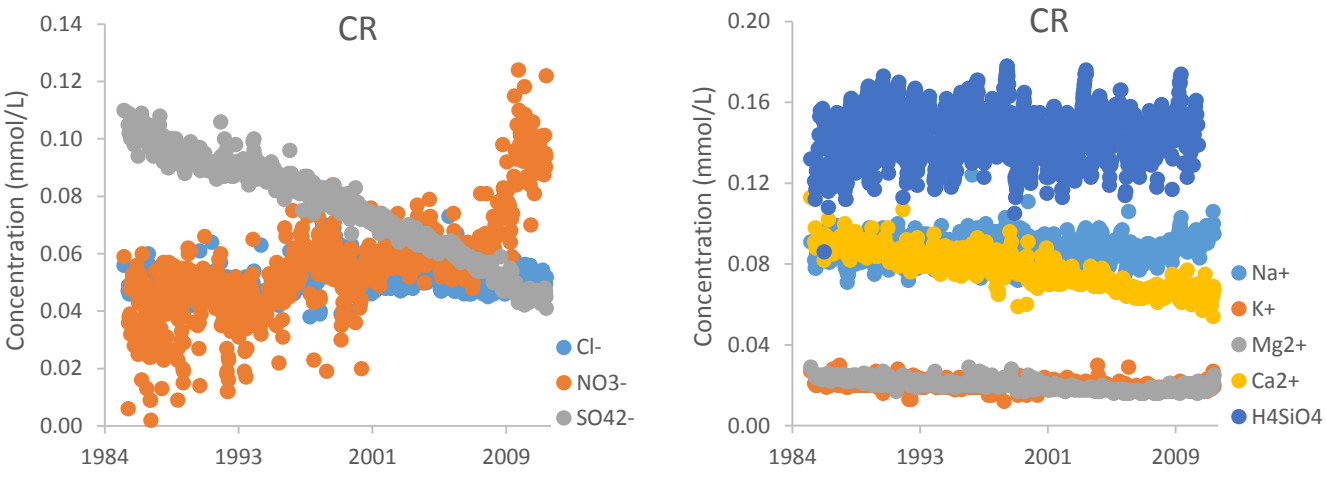
CR
Concentration (mmol/L)
0.14
0.12
0.10
0.08
0.06
0.04
0.02
0.00
1984
1993
2001
2009
Cl-
NO3-
SO42-
CR
Concentration (mmol/L)
0.20
0.16
0.12
0.08
0.04
0.00
1984
1993
2001
2009
Na+
K+
Mg2+
Ca2+
H4SiO4

Figure 3

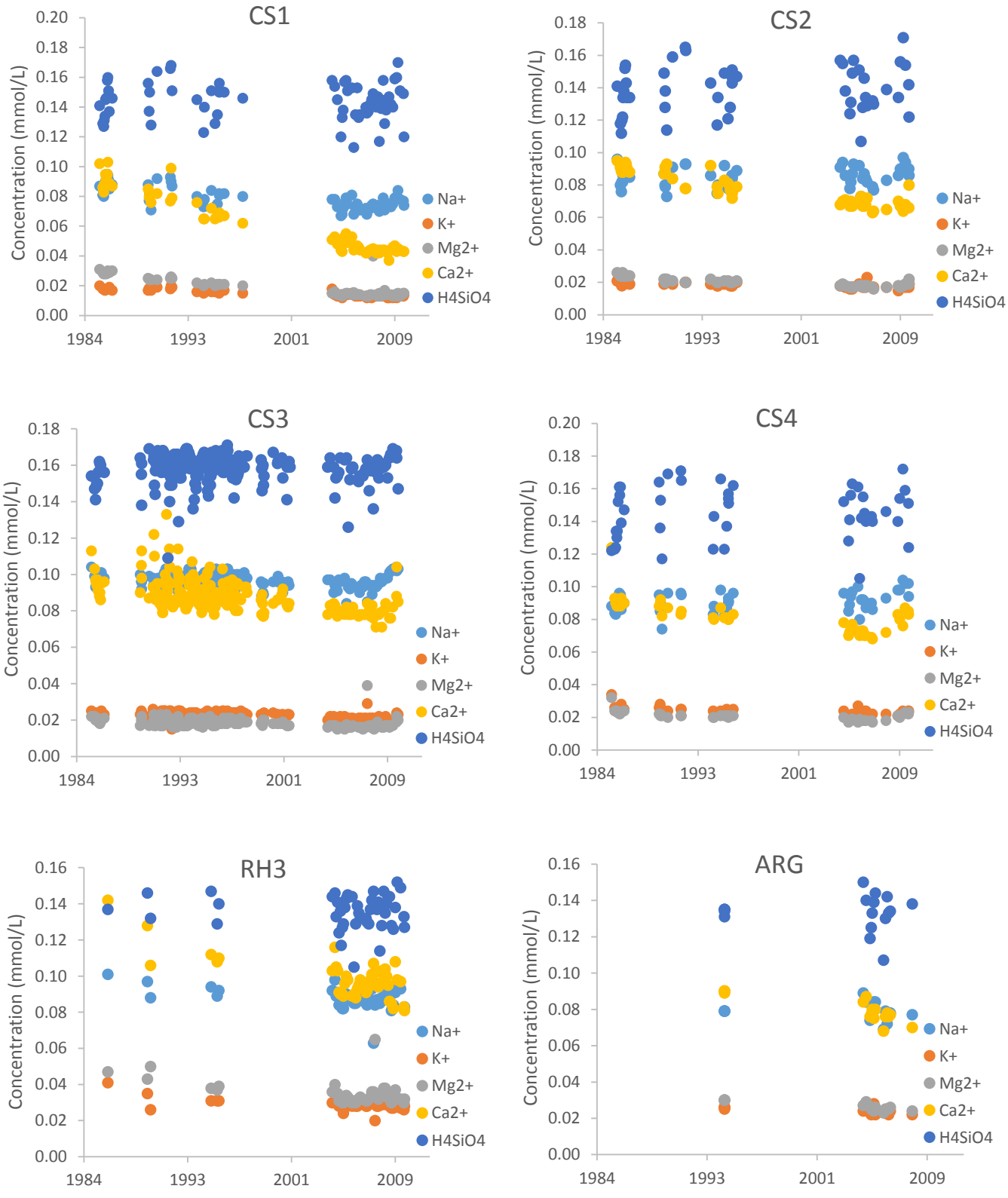
CS1
CS2
CS3
CS4
RH3
ARG
Concentration (mmol/L)
Na+
K+
Mg2+
Ca2+
H4SiO4
1984
1993
2001
2009

Figure 4

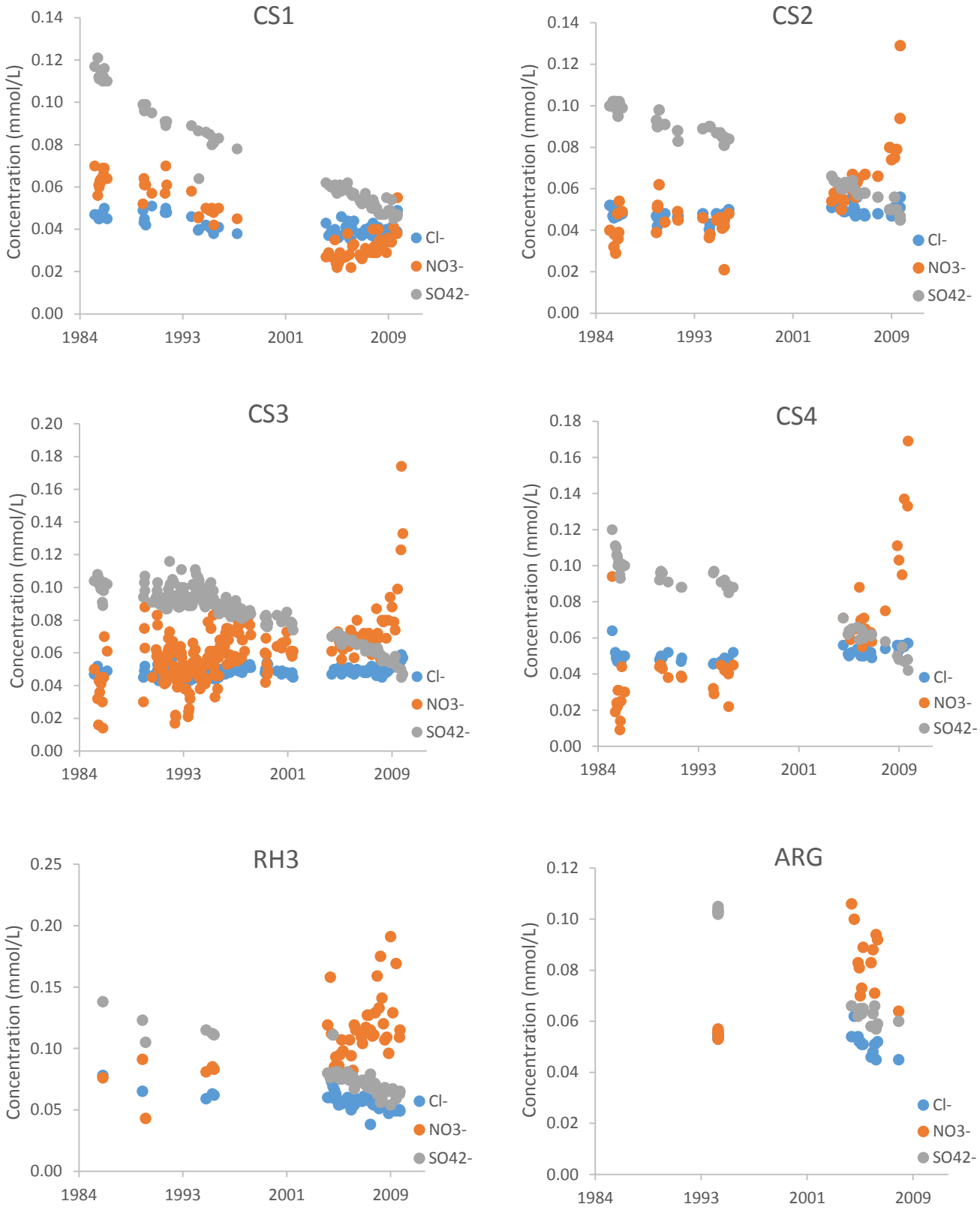
CS1
CS2
CS3
CS4
RH3
ARG
Concentration (mmol/L)
Cl-
NO3-
SO42-
1984
1993
2001
2009

Figure 5

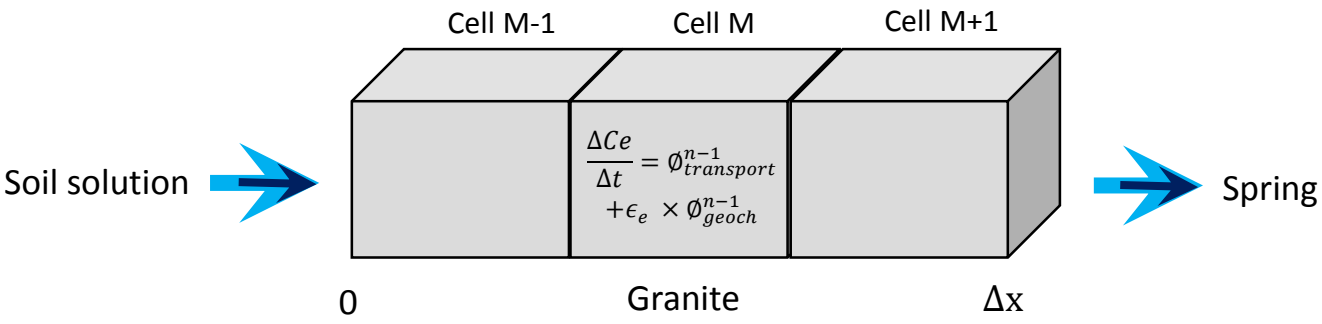
Cell M-1
Cell M
Cell M+1
Soil solution
$\frac{\Delta Ce}{\Delta t} = \emptyset_{transport}^{n-1} + \epsilon_e \times \emptyset_{geoch}^{n-1}$
Spring
0
Granite
Δx

Figure 6

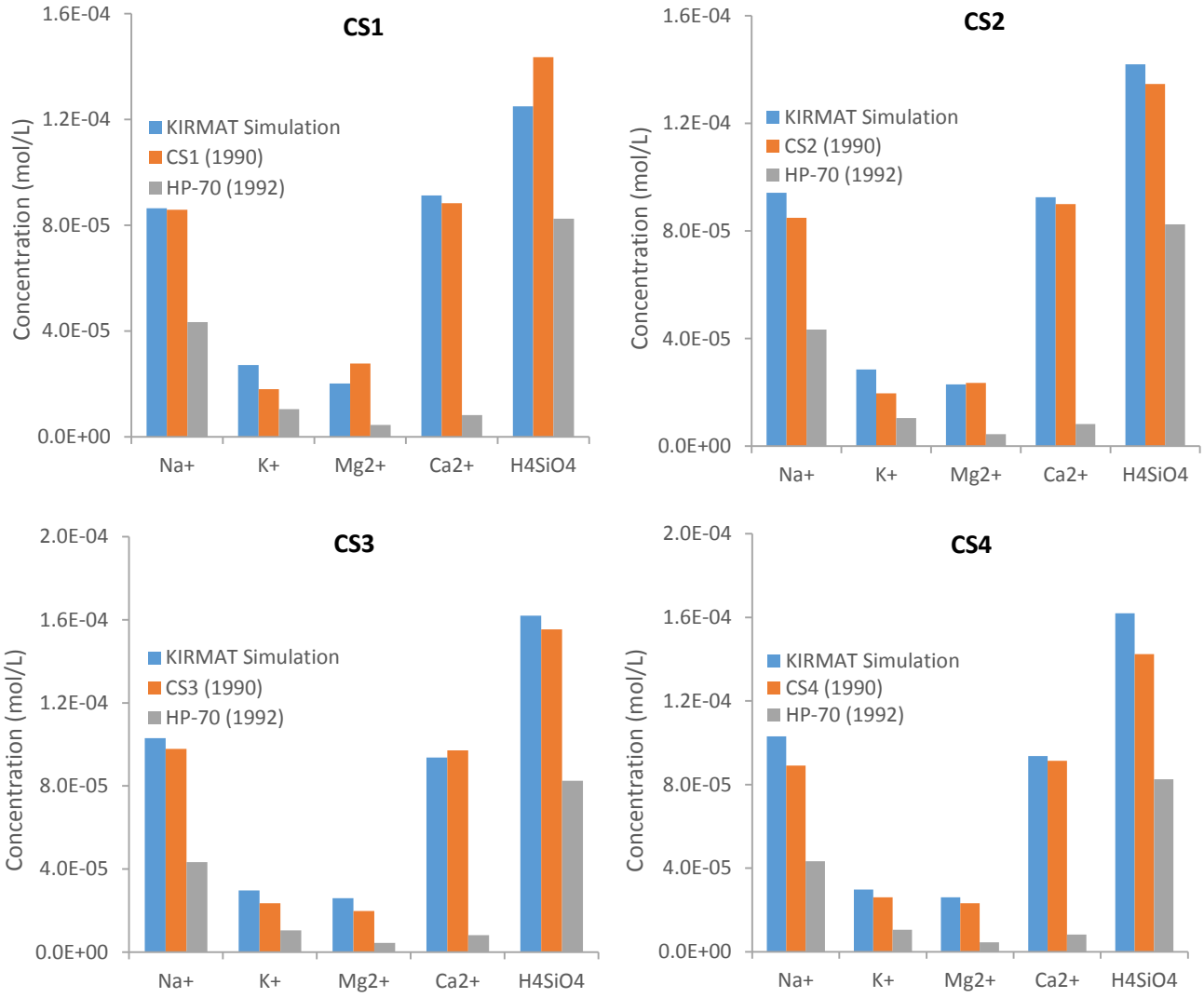
CS1
Concentration (mol/L)
1.6E-04
1.2E-04
8.0E-05
4.0E-05
0.0E+00
KIRMAT Simulation
CS1 (1990)
HP-70 (1992)
Na+
K+
Mg2+
Ca2+
H4SiO4
CS2
KIRMAT Simulation
CS2 (1990)
HP-70 (1992)
CS3
2.0E-04
KIRMAT Simulation
CS3 (1990)
HP-70 (1992)
CS4
KIRMAT Simulation
CS4 (1990)
HP-70 (1992)

Figure 7

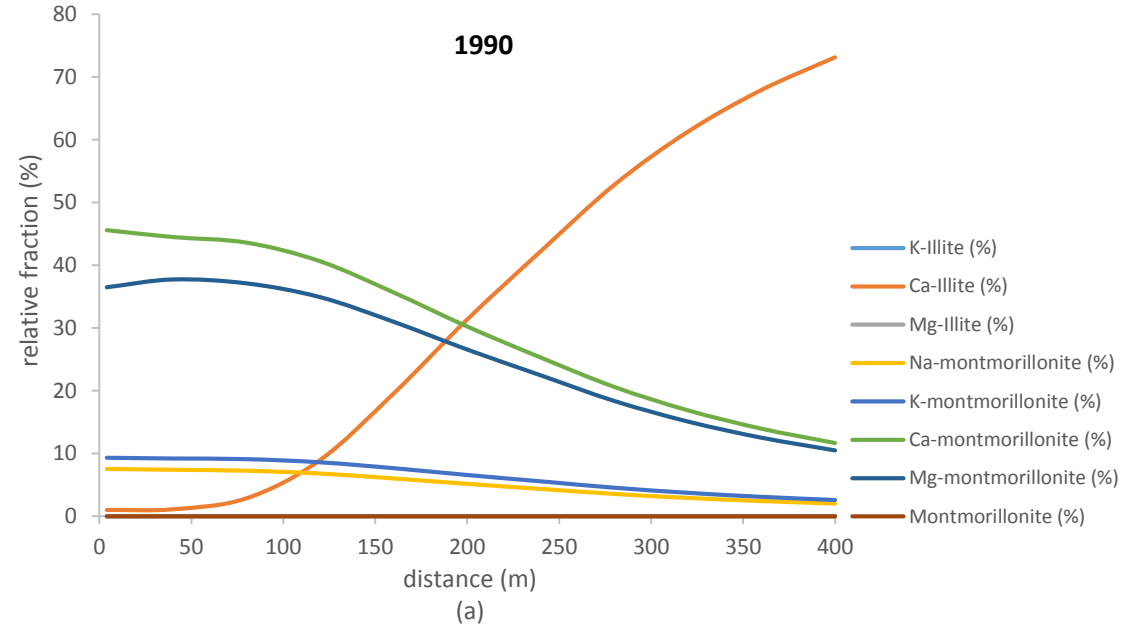
1990
relative fraction (%)
distance (m)
(a)
K-Illite (%)
Ca-Illite (%)
Mg-Illite (%)
Na-montmorillonite (%)
K-montmorillonite (%)
Ca-montmorillonite (%)
Mg-montmorillonite (%)
Montmorillonite (%)

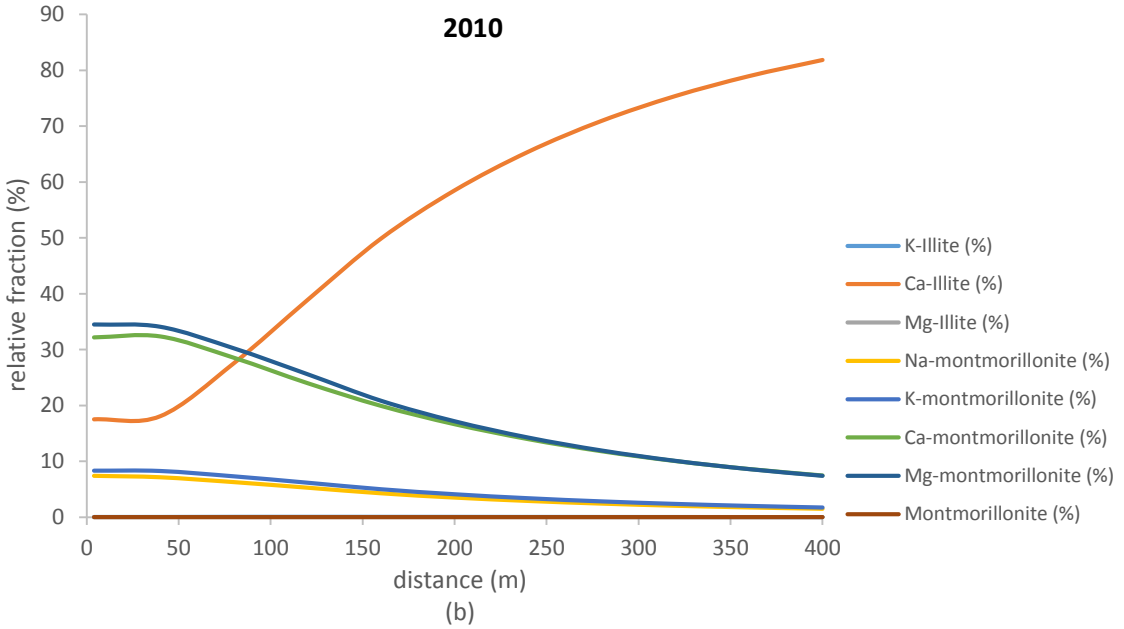
2010
relative fraction (%)
distance (m)
(b)
K-Illite (%)
Ca-Illite (%)
Mg-Illite (%)
Na-montmorillonite (%)
K-montmorillonite (%)
Ca-montmorillonite (%)
Mg-montmorillonite (%)
Montmorillonite (%)

Figure 8

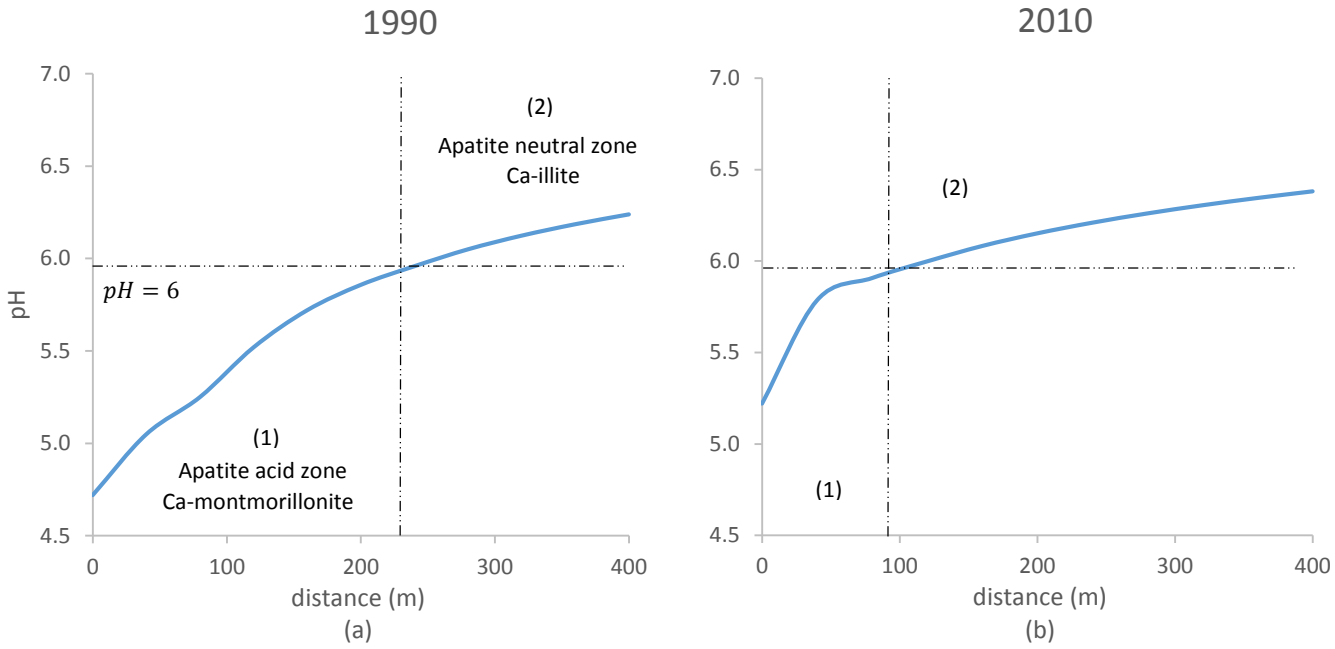
1990
2010
7.0
6.5
6.0
5.5
5.0
4.5
pH
$pH = 6$
(1)
Apatite acid zone
Ca-montmorillonite
(2)
Apatite neutral zone
Ca-illite
0
100
200
300
400
distance (m)
(a)
(b)

Figure 9

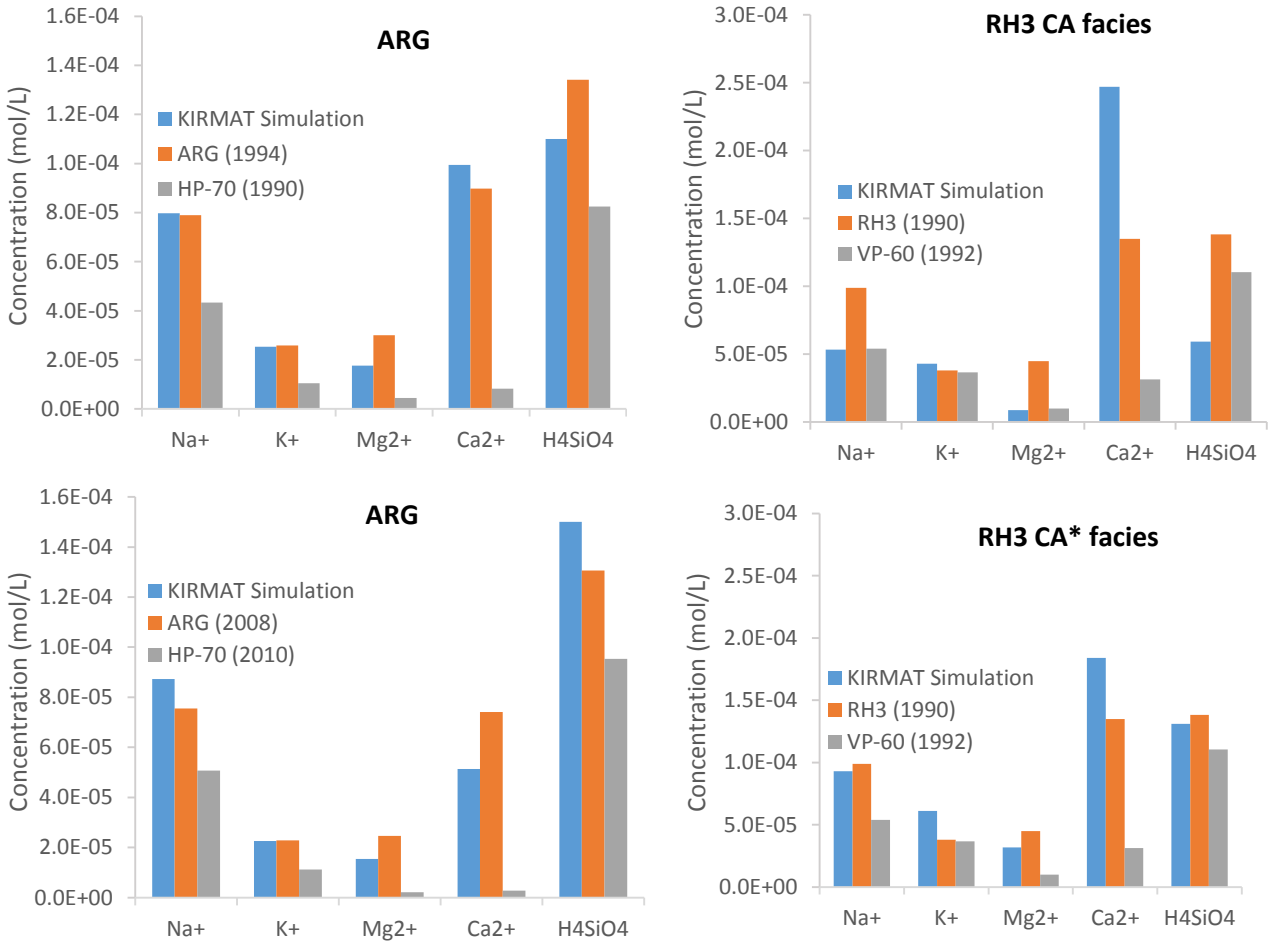
ARG
KIRMAT Simulation
ARG (1994)
HP-70 (1990)
Concentration (mol/L)
1.6E-04
1.4E-04
1.2E-04
1.0E-04
8.0E-05
6.0E-05
4.0E-05
2.0E-05
0.0E+00
Na+
K+
Mg2+
Ca2+
H4SiO4
RH3 CA facies
KIRMAT Simulation
RH3 (1990)
VP-60 (1992)
Concentration (mol/L)
3.0E-04
2.5E-04
2.0E-04
1.5E-04
1.0E-04
5.0E-05
0.0E+00
Na+
K+
Mg2+
Ca2+
H4SiO4
ARG
KIRMAT Simulation
ARG (2008)
HP-70 (2010)
Concentration (mol/L)
1.6E-04
1.4E-04
1.2E-04
1.0E-04
8.0E-05
6.0E-05
4.0E-05
2.0E-05
0.0E+00
Na+
K+
Mg2+
Ca2+
H4SiO4
RH3 CA* facies
KIRMAT Simulation
RH3 (1990)
VP-60 (1992)
Concentration (mol/L)
3.0E-04
2.5E-04
2.0E-04
1.5E-04
1.0E-04
5.0E-05
0.0E+00
Na+
K+
Mg2+
Ca2+
H4SiO4

Figure 10

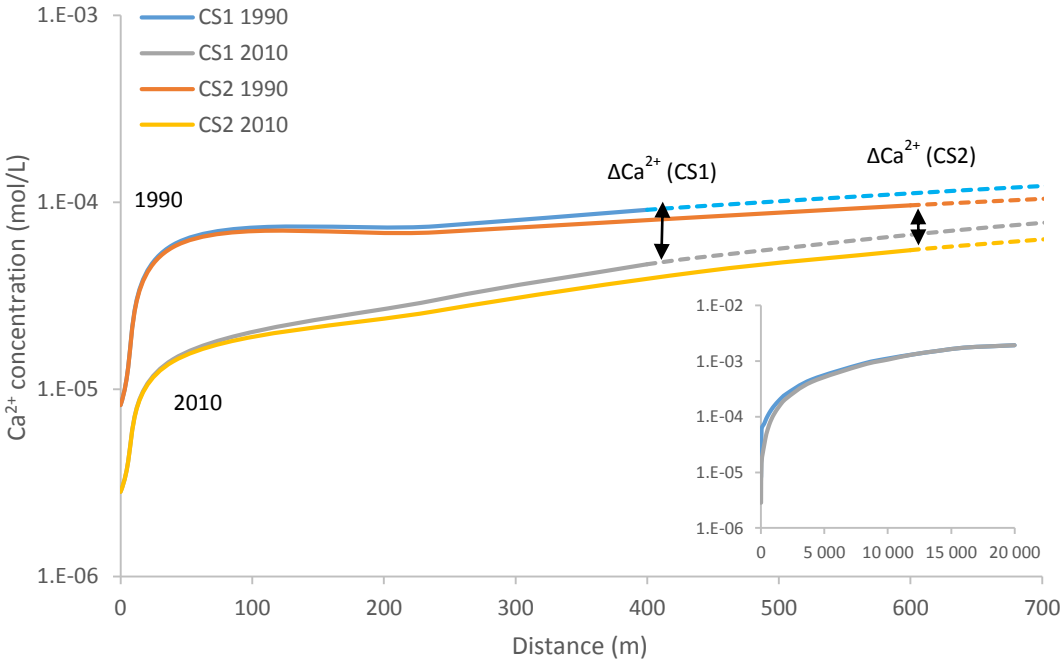
CS1 1990
CS1 2010
CS2 1990
CS2 2010
1990
2010
ΔCa2+ (CS1)
ΔCa2+ (CS2)
Ca2+ concentration (mol/L)
Distance (m)
1.E-03
1.E-04
1.E-05
1.E-06
0
100
200
300
400
500
600
700
1.E-02
1.E-03
1.E-04
1.E-05
1.E-06
0
5 000
10 000
15 000
20 000

Figure 11

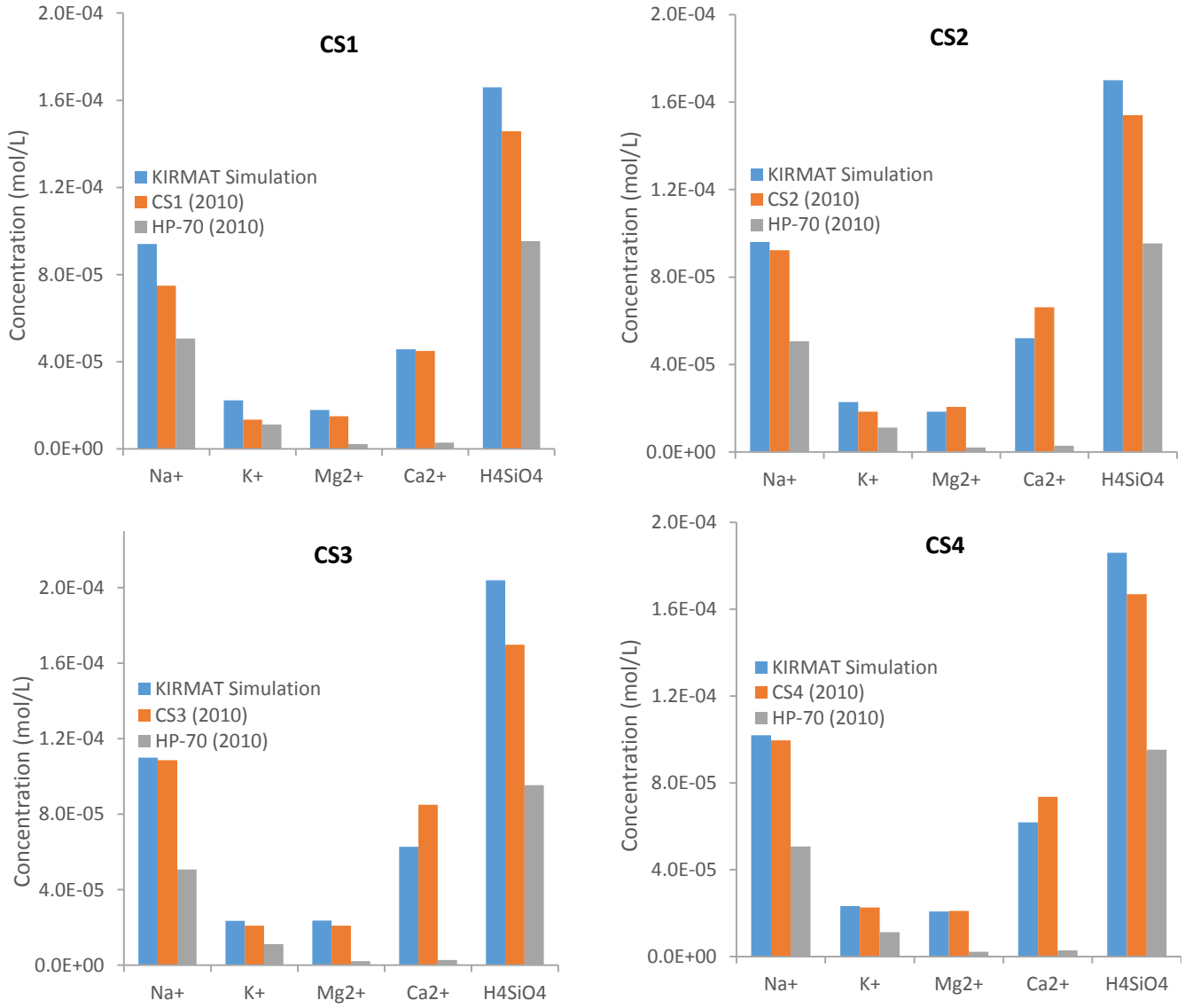
CS1
Concentration (mol/L)
2.0E-04
1.6E-04
1.2E-04
8.0E-05
4.0E-05
0.0E+00
KIRMAT Simulation
CS1 (2010)
HP-70 (2010)
Na+
K+
Mg2+
Ca2+
H4SiO4
CS2
KIRMAT Simulation
CS2 (2010)
HP-70 (2010)
CS3
KIRMAT Simulation
CS3 (2010)
HP-70 (2010)
CS4
KIRMAT Simulation
CS4 (2010)
HP-70 (2010)

Figure 12

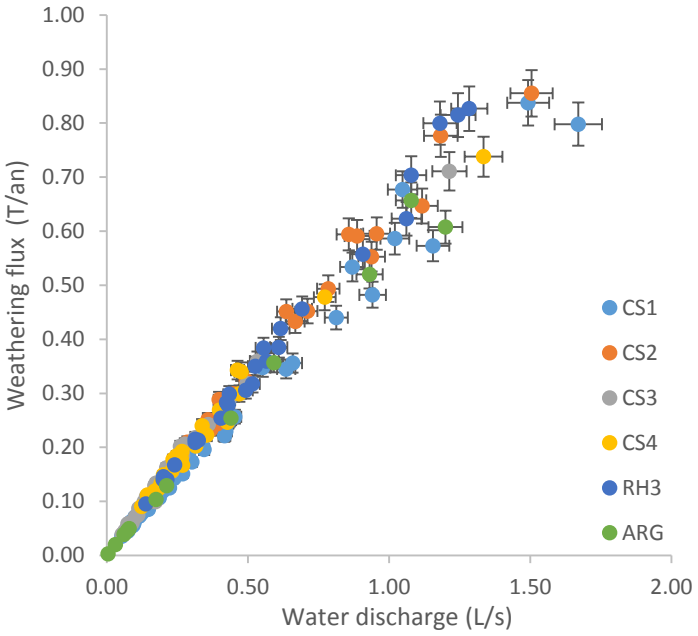
1.00
0.90
0.80
0.70
0.60
0.50
0.40
0.30
0.20
0.10
0.00
Weathering flux (T/an)
0.00
0.50
1.00
1.50
2.00
Water discharge (L/s)
CS1
CS2
CS3
CS4
RH3
ARG

Figure 13

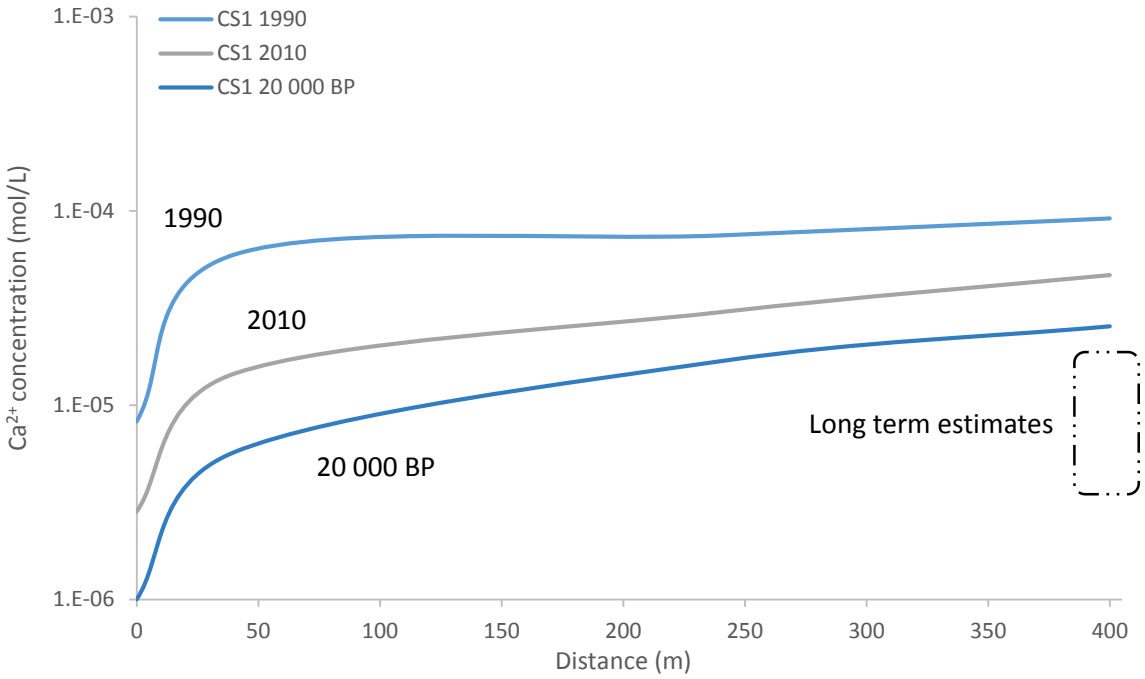
1.E-03
1.E-04
1.E-05
1.E-06
CS1 1990
CS1 2010
CS1 20 000 BP
1990
2010
20 000 BP
Long term estimates
Ca2+ concentration (mol/L)
0
50
100
150
200
250
300
350
400
Distance (m)

Figure 14

Mineral	Mass fraction (HPT facies) (%)	Reactive surface area (HPT facies) (m^2/kg H_2O)	Mass fraction (CA facies) (%)	Reactive surface area (CA facies) (m^2/kg H_2O)	Mass fraction (CA* facies) (%)	Reactive surface area (CA* facies) (m^2/kg H_2O)
Quartz	35	19.45	46	25.56	46	25.56
Albite	31	12.92	0	0	7	2.92
K-feldspar	22	5.16	5	1.17	5	1.17
Biotite	6	10.23	0	0	2	3.41
Muscovite	3	5.11	48	81.84	38	64.79
Anorthite	2	0.83	0	0	0	0
Apatite	0.5	0.02	0.3	0.004	0.3	0.004
Illite	0.5	18.75	0.7	26.26	1.7	63.77

Table 1

(T/km²/yr)	Na^+	K^+	Mg^{2+}	Ca^{2+}	H_4SiO_4
CS1 spring					
(F)	0.30 ± 0.06	0.10 ± 0.02	0.07 ± 0.02	0.38 ± 0.07	2.29 ± 0.45
(A)	0.08 ± 0.02	0	0.04 ± 0.01	0.24 ± 0.06	2.23 ± 0.55
(B)	0.10 ± 0.03	0.01 ± 0.004	0.05 ± 0.02	0.31 ± 0.09	2.34 ± 0.58
(C)	0.10 ± 0.03	0.07 ± 0.028	0.06 ± 0.03	0.37 ± 0.11	2.37 ± 0.59
CS2 spring					
(F)	0.34 ± 0.07	0.13 ± 0.03	0.08 ± 0.02	0.53 ± 0.10	2.26 ± 0.45
(A)	0.10 ± 0.02	0	0.05 ± 0.01	0.33 ± 0.08	2.20 ± 0.55
(B)	0.11 ± 0.03	0.02 ± 0.008	0.06 ± 0.02	0.43 ± 0.13	2.31 ± 0.57
(C)	0.12 ± 0.04	0.09 ± 0.036	0.07 ± 0.02	0.52 ± 0.16	2.34 ± 0.58
CS3 spring					
(F)	0.28 ± 0.06	0.11 ± 0.02	0.06 ± 0.01	0.45 ± 0.09	2.76 ± 0.55
(A)	0.08 ± 0.02	0	0.04 ± 0.01	0.28 ± 0.07	2.69 ± 0.67
(B)	0.09 ± 0.03	0.02 ± 0.008	0.04 ± 0.01	0.37 ± 0.11	2.83 ± 0.70
(C)	0.10 ± 0.03	0.07 ± 0.028	0.05 ± 0.02	0.44 ± 0.13	2.86 ± 0.71
CS4 spring					
(F)	0.32 ± 0.07	0.14 ± 0.03	0.07 ± 0.02	0.47 ± 0.10	2.09 ± 0.52
(A)	0.09 ± 0.02	0	0.04 ± 0.01	0.29 ± 0.07	2.03 ± 0.51
(B)	0.11 ± 0.03	0.02 ± 0.008	0.05 ± 0.02	0.38 ± 0.11	2.14 ± 0.54
(C)	0.11 ± 0.03	0.09 ± 0.036	0.06 ± 0.02	0.46 ± 0.14	2.17 ± 0.54
Regolith profile	0.22 ± 0.14	0.39 ± 0.25	0.02 ± 0.01	0.04 ± 0.02	3 ± 2

Table 2

Electronic Annex Figures

Figure 1: concentration time evolutions of cations (Na^+, K^+, Ca^{2+}, Mg^{2+}) for the PA rainfalls collected at the summit of the Strengbach watershed from 1986 to 2010.

Figure 2: concentration time evolutions of anions and dissolved silica (SO_4^{2-}, NO_3^-, Cl^-, H_4SiO_4) for the PA rainfalls collected at the summit of the Strengbach watershed from 1986 to 2010.

Figure 3: measured pH for the soil solutions VP-60, HP-70, and for the PA rainfalls and the CR waters from 1986 to 2010.

Figure 4: concentration time evolutions of cations (Na^+, K^+, Ca^{2+}, Mg^{2+}) for the soil solution VP-60 collected at the spruce site from 1992 to 2010.

Figure 5: concentration time evolutions of cations (Na^+, K^+, Ca^{2+}, Mg^{2+}) for the soil solution HP-70 collected at the beech site from 1992 to 2010.

Figure 6: concentration time evolutions of anions and dissolved silica (SO_4^{2-}, NO_3^-, Cl^-, H_4SiO_4) for the soil solution VP-60 collected at the spruce site from 1992 to 2010.

Figure 7: concentration time evolutions of anions and dissolved silica (SO_4^{2-}, NO_3^-, Cl^-, H_4SiO_4) for the soil solution HP-70 collected at the beech site from 1992 to 2010.

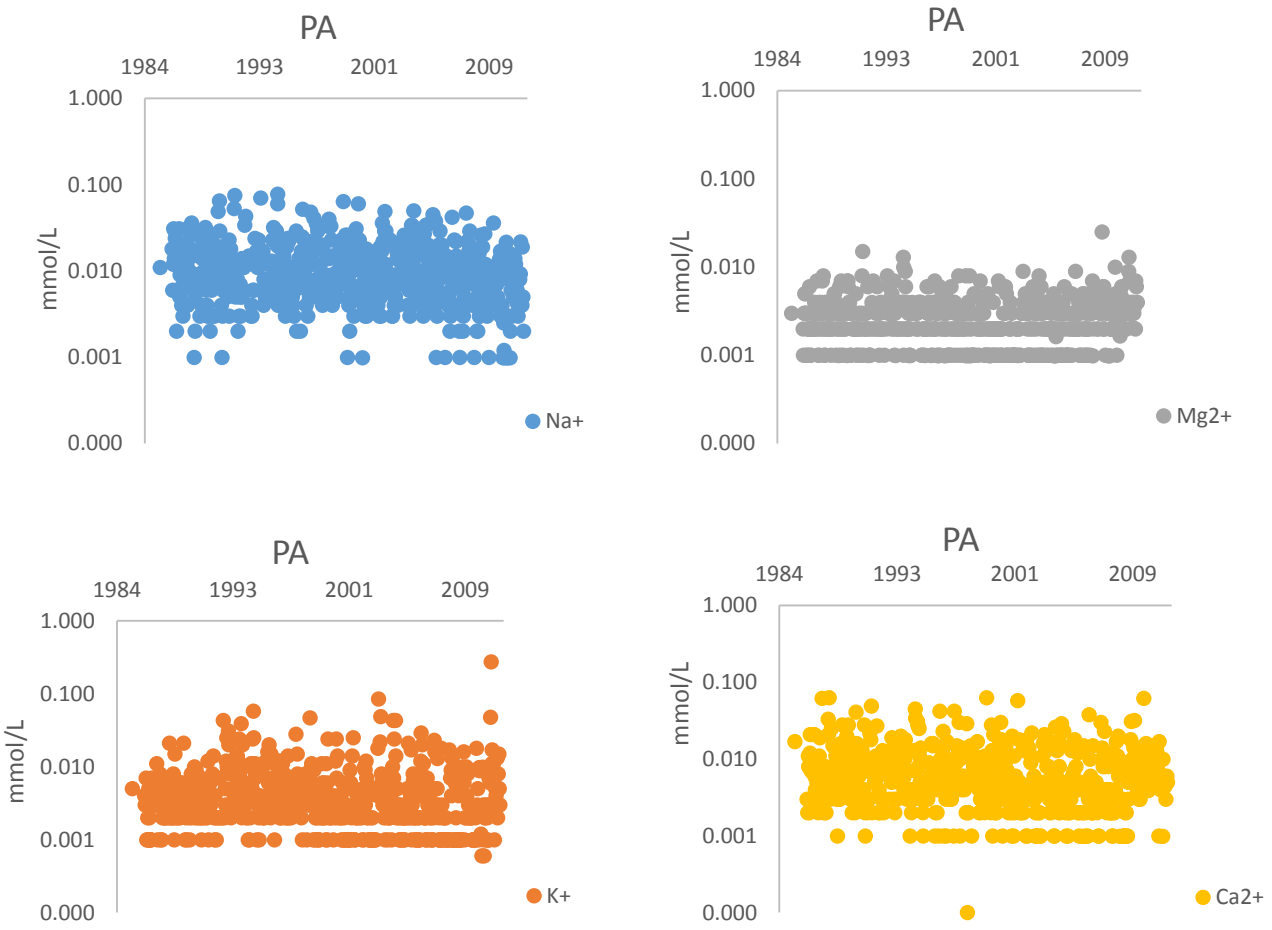
PA
1984
1993
2001
2009
1.000
0.100
0.010
0.001
0.000
mmol/L
Na+
PA
1984
1993
2001
2009
1.000
0.100
0.010
0.001
0.000
mmol/L
Mg2+
PA
1984
1993
2001
2009
1.000
0.100
0.010
0.001
0.000
mmol/L
K+
PA
1984
1993
2001
2009
1.000
0.100
0.010
0.001
0.000
mmol/L
Ca2+

Figure 1


PA
1984
1993
2001
2009
1.000
0.100
0.010
0.001
mmol/L
SO42-
PA
1984
1993
2001
2009
1.000
0.100
0.010
0.001
0.000
mmol/L
NO3-
PA
1984
1993
2001
2009
1.000
0.100
0.010
0.001
mmol/L
Cl-
PA
1984
1993
2001
2009
0.1000
0.0100
0.0010
0.0001
mmol/L
H4SiO4

Figure 2


VP-60
6.0
5.5
5.0
4.5
4.0
3.5
3.0
1984
1993
2001
2009
pH
HP-70
7.0
6.5
6.0
5.5
5.0
4.5
4.0
3.5
3.0
1984
1993
2001
2009
pH
PA
8.0
7.0
6.0
5.0
4.0
3.0
2.0
1984
1993
2001
2009
pH
CR
7.5
7.0
6.5
6.0
5.5
5.0
1984
1993
2001
2009
pH

Figure 3

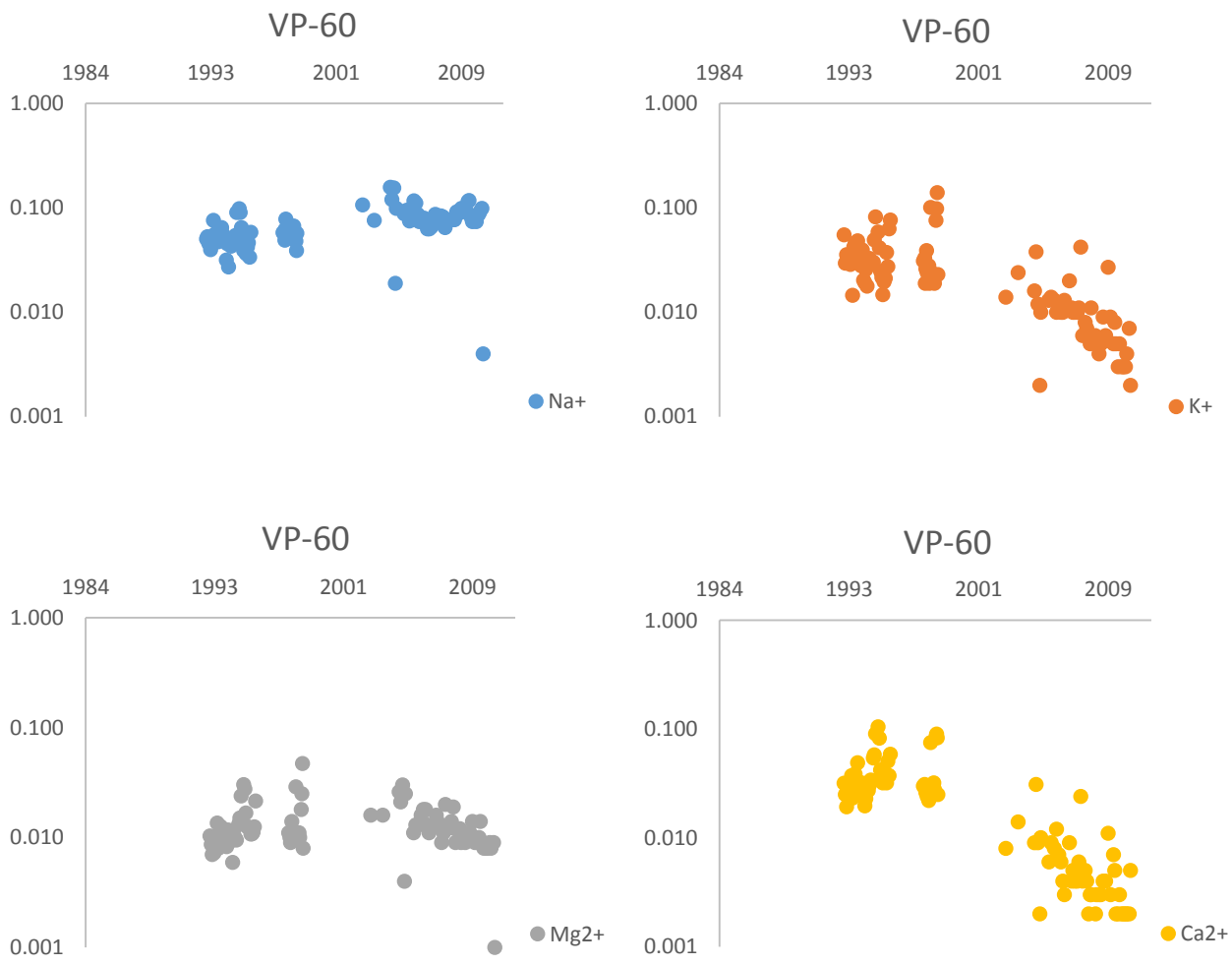
VP-60
1984
1993
2001
2009
1.000
0.100
0.010
0.001
Na+
VP-60
1984
1993
2001
2009
1.000
0.100
0.010
0.001
K+
VP-60
1984
1993
2001
2009
1.000
0.100
0.010
0.001
Mg2+
VP-60
1984
1993
2001
2009
1.000
0.100
0.010
0.001
Ca2+

Figure 4

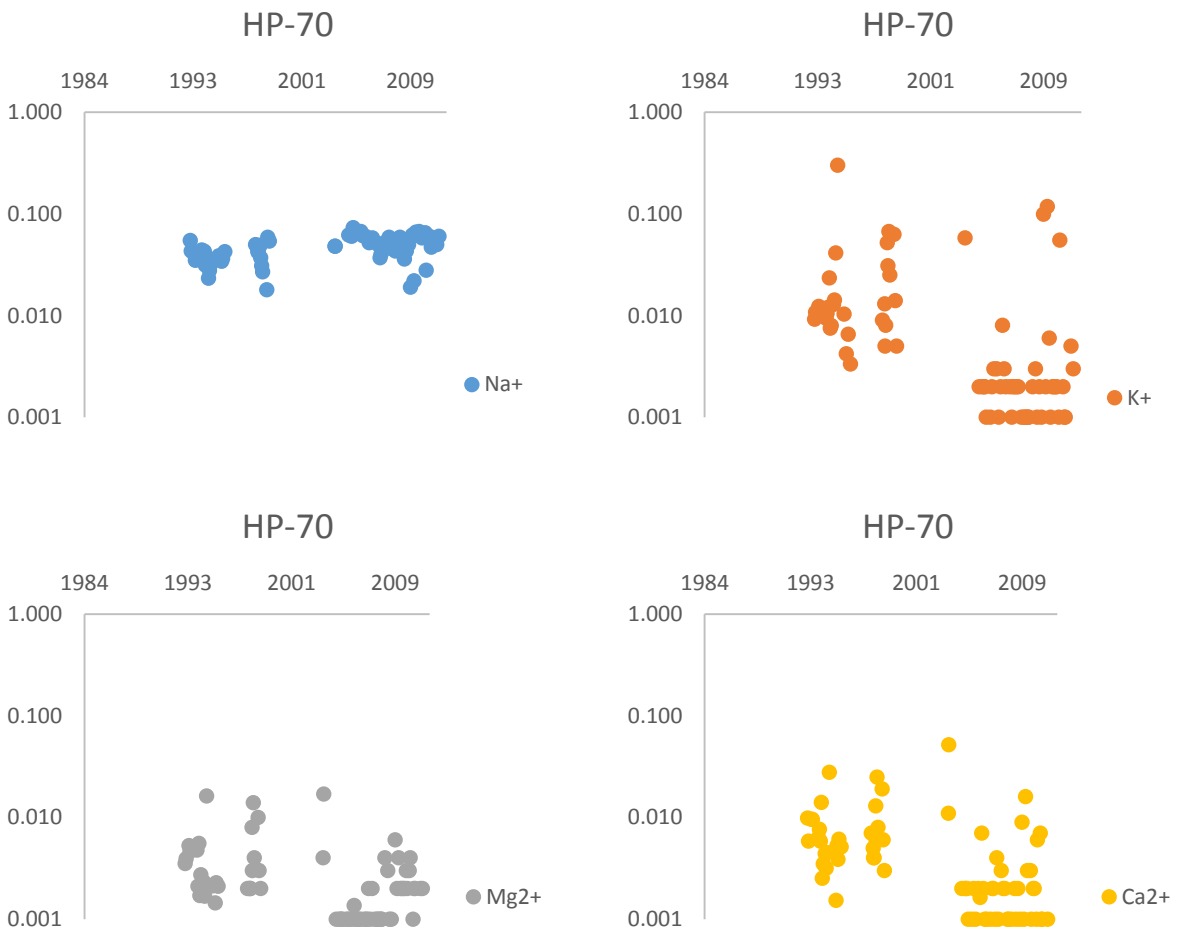
HP-70
1984
1993
2001
2009
1.000
0.100
0.010
0.001
Na+
HP-70
1984
1993
2001
2009
1.000
0.100
0.010
0.001
K+
HP-70
1984
1993
2001
2009
1.000
0.100
0.010
0.001
Mg2+
HP-70
1984
1993
2001
2009
1.000
0.100
0.010
0.001
Ca2+

Figure 5

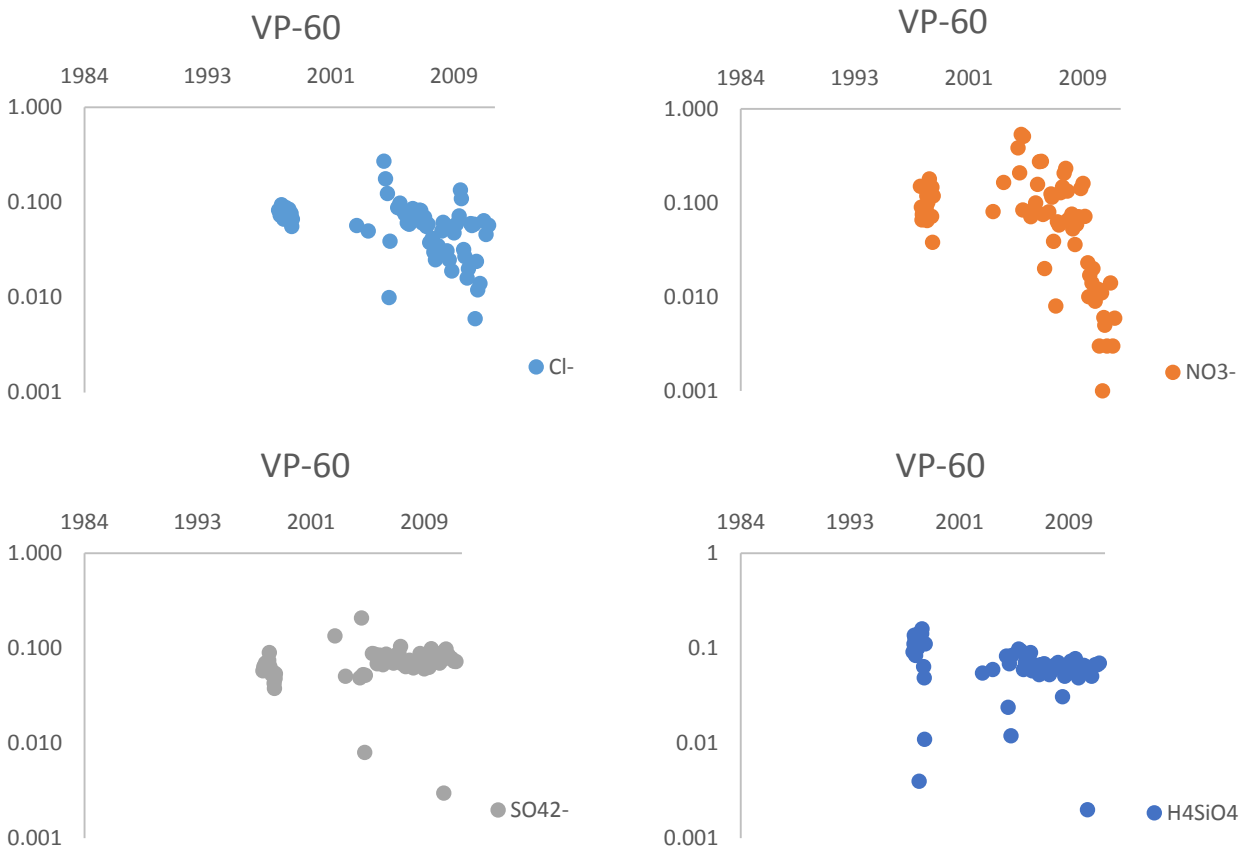
VP-60
1984
1993
2001
2009
1.000
0.100
0.010
0.001
Cl-
VP-60
1984
1993
2001
2009
1.000
0.100
0.010
0.001
NO3-
VP-60
1984
1993
2001
2009
1.000
0.100
0.010
0.001
SO42-
VP-60
1984
1993
2001
2009
1
0.1
0.01
0.001
H4SiO4

Figure 6

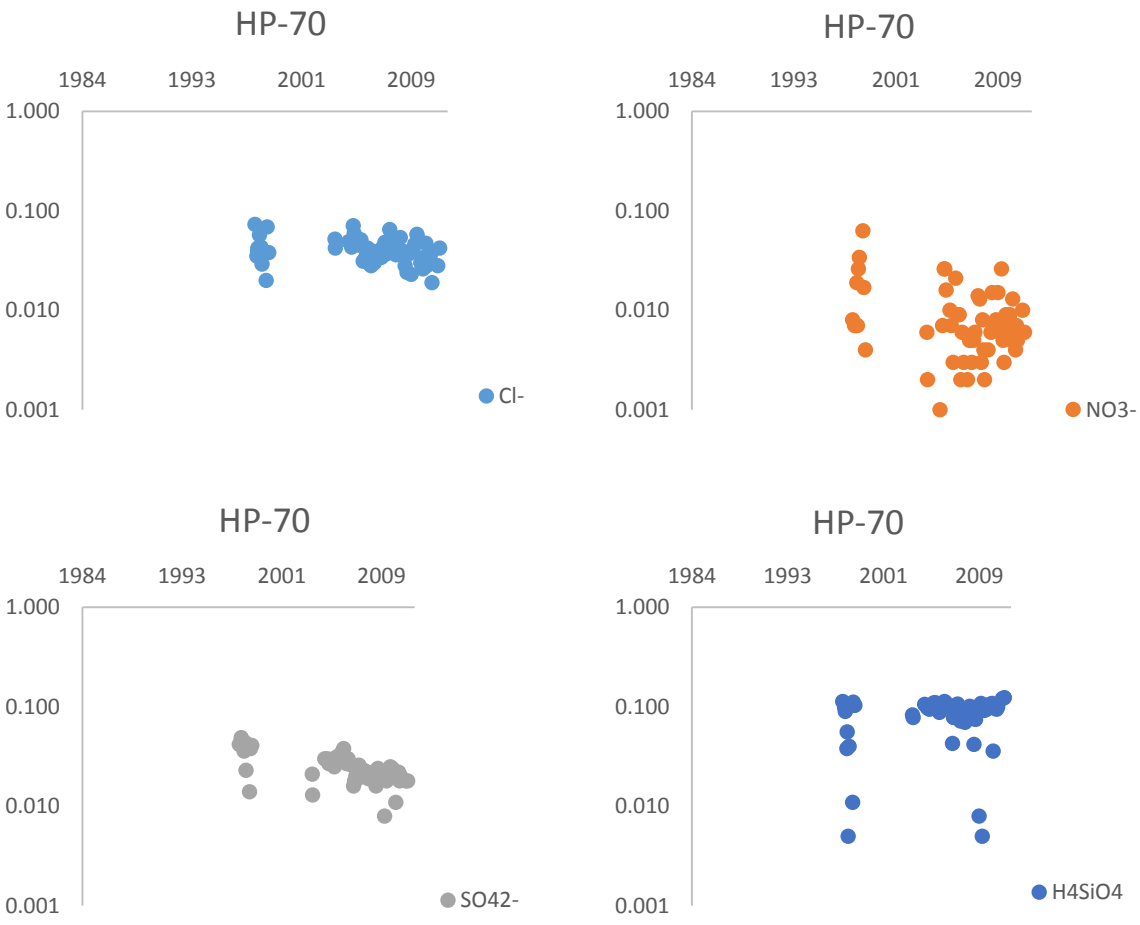
HP-70
1984
1993
2001
2009
1.000
0.100
0.010
0.001
Cl-
HP-70
1984
1993
2001
2009
1.000
0.100
0.010
0.001
NO3-
HP-70
1984
1993
2001
2009
1.000
0.100
0.010
0.001
SO42-
HP-70
1984
1993
2001
2009
1.000
0.100
0.010
0.001
H4SiO4

Figure 7